Cape Peninsula
University of Technology

EFFECTIVENESS FACTOR MODEL DEVELOPMENT AND VALIDATION FOR AN ETHYLENE PHOTOCATALYTIC DEGRADATION REACTOR BASED ON ROBIN BOUNDARY CONDITIONS

by

MAKIWE ANNETTE NKOHLA

Thesis submitted in fulfilment of the requirements for the degree

Doctor of Engineering: Chemical Engineering

in The

Faculty of Engineering and The Built Environment

at the

Cape Peninsula University of Technology

Supervisor:	**Dr B Godongwana**
Co-supervisors:	**Prof VG Fester**
	Dr O Caleb
	Dr P Mathabe

Bellville
April 2025

DECLARATION

I, Makiwe Annette Nkohla, declare that the contents of this thesis represent my own unaided work, and that the thesis has not previously been submitted for academic examination towards any qualification. Furthermore, it represents my own opinions and not necessarily those of the Cape Peninsula University of Technology.

Signed **Date** **23 April 2025**

ABSTRACT

The accumulation of excessive amounts of ethylene, a naturally occurring plant hormone in fruit storage is one of the reasons for the loss of produce in the fruit and vegetable industry. Photocatalytic Oxidation (PCO) is a method that can be used to reduce ethylene around the fruit storage atmosphere. PCO has shown promising results in reducing ethylene concentration based on laboratory scale. However, the commercial application of PCO is hindered by the lack of rigorous mass transfer mathematical models required for optimum reactor design, scalable to an industrial size.

In the current study, a model of the catalysed reaction kinetics is developed. The performance of the PCO reactor is characterized by means of the effectiveness factor, which is a ratio of the actual reaction rate to the theoretical rate in the absence of mass transfer limitation. An analytical expression of the effectiveness factor that accounts for external mass transfer limitations is presented. The solution is based on Robin boundary conditions, and is a function of the Sherwood number, the Thiele modulus, and dimensions of the PCO reactor and catalyst. Regions highlighting free diffusion, diffusion limitations, and external mass transfer limitations are identified based on the Thiele Modulus and the Sherwood number. At low values of the Sherwood number, the internal diffusion and reaction rate-limiting regions are surpassed by the external mass transfer limitations. A cut-off value of the Sherwood number below which external mass transfer limitations cannot be ignored is 0.55. The evaluation of the model showed that under conditions of Dirichlet the model converges to literature models from similar studies. This 1-D model evaluated the Sherwood number across a broad scope and accounted for a broader range of limitations associated with immobilized photocatalytic films.

The developed mass transfer and effectiveness factor models were validated by means of kinetic experiments in a photocatalytic reactor using ethylene as the model pollutant. The experimental reaction rate was then compared to the theoretical reaction rate as predicted by the model. The results show a good agreement between the model predictions and the measured rates. Plots of Damköhler numbers and conversion for continuous stirred tank and plug flow reactors are presented to show the application of the model in the design and scaling up of photocatalytic reactors. A device for measuring the concentration of ethylene was built using Arduino Uno (microprocessor) and MQ3 gas sensors.

ACKNOWLEDGEMENTS

I wish to thank:

- My supervisor, Dr B. Godongwana, for his guidance, support, and expertise, without whom this thesis would not have been completed.
- My co-supervisor, Prof V.G. Fester, for her guidance, her compassionate support kept me going despite the challenges.
- My co-supervisors, Dr O Caleb and Dr P Mathabe, for the collaboration with the Agricultural Research Council (Infruitec), project resources and guidance.
- Chemical Engineering Workshop personnel, Mr Alwyn Bester, for technical support.
- Chemical Engineering Laboratory Technicians, Mrs Hannelene Small, and Mr Derrick Dlamini laboratory resources.
- Senior Laboratory Technician (Electrical, Electronic & Computer Engineering), Mr Christopher Wills, and his Inservice Trainee (Athabulela) for their help with the UV lamp connection circuit.
- Mr Richard J Du Toit for his help with the experimental setup and experiments.
- My brother, Samkelo Nkohla, for his help with his technical expertise.
- My daughter, Lintle Sibabalwe Nkohla, for her understanding and support.
- My mother, my brothers, and my sister, for their unwavering support.

The financial assistance of NRF, Thuthuka, towards this research is acknowledged. Opinions expressed in this thesis and the conclusions arrived at, are those of the author, and are not necessarily to be attributed to the National Research Foundation.

DEDICATION

This thesis is dedicated to my late aunt, Ntombekhaya Victoria Mpofana, who has been my emotional support and encouragement throughout my personal life and academic journey.

TABLE OF CONTENTS

LIST OF FIGURES

LIST OF TABLES

ABBREVIATIONS AND ACRONYMS

Abbreviation/Acronym	
LEDs	Light Emitting Diodes
CSTR	Continuous Stirred Tank Reactor
PFR	Plug Flow Reactor
UV	Ultraviolet
MFC	Mass Flow Controller
SEM	Scanning Electron Microscopy
VOC/ VOCs	Volatile Organic Compound(s)
TiO_2	Titanium dioxide
P25	TiO_2 mixture containing Anatase and Rutile phases
SFF	Silica Fiber Felts
C_2H_4	Ethylene gas
H_2O	Water
CO_2	Carbon dioxide

GLOSSARY

Term	
Band gap energy (E_b)	The difference between the filled valence band and the empty conduction band of the photocatalyst, in the order of a few electron volts.
Climacteric fruits	Fruits that can ripen after being harvested. (e.g. apples, apricots, avocados, bananas, peaches, plums, and tomatoes)
Control	In this study 'control' refers to a fruit storage in which there is no means for reducing ethylene gas.
Perturbation	A semi-analytical method that rely on there being a parameter in the problem that is relatively small.
Photocatalysis	A change in the rate of chemical reactions or their generation under the action of light in the presence of substances called photocatalyst.
Photocatalyst	A material which absorbs light to bring it to higher energy level and provides such energy to a reacting substance to make a chemical reaction occur.
Senescence	The process of ageing in plants, fruits and vegetables.
Respiration	The process of consuming oxygen and giving off carbon dioxide, water and heat. Respiration rate is an important fruit quality parameter as it is related to the loss of water.
Dimensionless numbers	
Effectiveness factor (η)	The ratio of the actual reaction rate to the ideal reaction rate that would be achieved if there were no diffusion limitations within a catalyst particle. It is used to measure the effectiveness of a catalyst particle in facilitating a chemical reaction, considering mass transfer effects within the catalyst particle (diffusion) and the effects of mass transfer from the bulk fluid to the catalyst surface (convection).

Optical Thickness (Δ)	The product of the thickness of the catalyst layer and its absorption coefficient, which indicates the distance that the photons must travel to be absorbed by the catalyst coating.
Peclet number (*Pe*)	The ratio of the rate of advection to the rate of diffusion used in fluid dynamics to measure the comparative significance of convective to diffusive mass transport. If *Pe* is much higher than *Sh*, the mass transfer is likely limited by convective transport.
Schmidt number (Sc)	The ratio of fluid kinematic viscosity to fluid mass diffusivity that determines the significance of momentum and mass transport by diffusion in a fluid flow operation.
Sherwood number (*Sh*)	The ratio of convective mass transfer to diffusive mass transfer, where high *Sh* indicates convection-dominated mass transfer, while low *Sh* indicates diffusion-dominated mass transfer. If *Sh* is much higher than *Pe*, the mass transfer is likely limited by diffusion.
Thiele Modulus (ϕ)	The ratio of the reaction rate to the diffusion rate within a catalyst particle. It is used to determine the significant reaction limiting steps between reaction kinetics and mass transport.

PUBLICATIONS EMANATING FROM THIS WORK

Nkohla, M.A., Godongwana, B., Fester, V.G. & Caleb, O.J. 2023. An analytical solution of the effectiveness factor of photocatalytic reactors based on Robin boundary conditions. *Chemical Engineering Journal Advances*, 14.

CHAPTER 1
INTRODUCTION

1.1 Background to the study

The accumulation of excessive amounts of ethylene, a naturally occurring plant hormone in fruit storage is one of the reasons for the loss of produce in the fruit and vegetable industry (Nayik & Muzaffar, 2014). This is because the fruit quality deteriorates due to over-ripening, increased pathogen susceptibility, physiological disorders, and senescence caused by over-exposure to ethylene (Martínez-Romero *et al*., 2007). Methods for combatting ethylene during postharvest storage will not only ensure food security, thereby reducing losses, but also impact the environment due to reduced waste that would have been dumped in the landfills, polluting the soil and the air.

Wills (2015) has given a limit of ethylene levels lower than 0.001 μLL^{-1} for the longest postharvest life without the physiological effect of ethylene on fruits. Some studies (Keller *et al*., 2013; Blanke, 2014; Namrata Pathak *et al*., 2017) have shown that the release of ethylene during postharvest storage by most fruits, especially climacteric fruits exceed this limit. Table 1.1 shows the ethylene production rates for some fruits, including their reaction to ethylene exposure.

Table1. 1: Ethylene production rates, sensitivity levels, and principal effects for some fresh commodities (Keller *et al*., 2013)

Fresh produce type	Ethylene production rate ($\mu Lkg^{-1}h^{-1}$)	Ethylene sensitivity[a]	Principal reaction to ethylene
Cherries	Very low < 0.1	L	Softening
Potatoes	Very low < 0.1	M	Sprouting
Cut flowers	Very low < 0.1	H	Sleepiness, leaf curl
Cucumber	Low 0.1 – 1.0	H	Yellowing
Banana	Moderate 1.0 - 10	H	Decay
Tomato	Moderate 1.0 - 10	H	Shrink, decay
Apricot, avocado	High 10 - 100	H	Decay
Apple	Very high > 100	H	Scald, lose crunch
Passion fruit	Very high > 100	H	Decay

[a]Ethylene sensitivity (ppm): H = high (0.01 – 0.5); M = moderate (0.5 – 3); L = low (3 – 5).

It is evident from Table 1.1 that climacteric fruits such as bananas, tomatoes, apricots, apples, etc., produce high levels of ethylene and are also highly sensitive to ethylene exposure, which implies that they can be affected negatively by very low concentrations of ethylene. A recent study by Pathak *et al*. (2019) revealed that the ethylene concentration increased to 70 μLL^{-1} when apples were stored in an airtight chamber at 1°C for a period of 8 days. Thus, there is a need to prevent ethylene accumulation in fruit storage facilities. For effective long-distance transport and subsequent storage, climacteric fruit must be held in a low (below 1.0–0.01 μLL^{-1}) ethylene environment (Terry *et al*., 2007). In addition to prolonging the storage life of the produce, Wills *et al*. (2014) have shown that by maintaining ethylene at low levels, it could be feasible to transport bananas without refrigeration. This leads to reduced energy utilization by the refrigeration system, even in stationery storage facilities.

Many scrubbing compounds have been employed to prevent the accumulation of ethylene, such as the adsorbents/ sorbents (activated carbon, palladium, zeolite) and the oxidizers (Potassium permanganate, and ozone) (Bailén *et al*., 2006; Martínez-Romero *et al*., 2007; Syamsu *et al*., 2016; Tirgar *et al*., 2018). These are used primarily in packaging films or sachets and have been shown to be useful. Other ethylene removal methods include biofiltration, air ventilation, and high temperature catalytic oxidation (Blidi *et al*., 1993; Fu *et al*., 2011; Keller *et al*., 2013).

These methods are efficient in their own respect, and are used commercially, however for long-term storage they may have some limitations as some materials, such as palladium (Tirgar *et al*., 2018), are expensive, get saturated rapidly, and thus require frequent replacement, resulting in increased waste disposal costs. Thus, their application in large volume storage containers may be limited. Processes like biofiltration and high temperature catalytic oxidation are well established although require long time exposure and involve high energy requirements, respectively. Ventilation is currently the most commonly used and efficient method for removing ethylene in fruit storage, depending on the location of the storage facility, there is possible contamination of outside air by ethylene (Keller *et al*., 2013). Thus, in addition to these tried and tested methods there is a need for more robust techniques that will offer quick ethylene reduction and longer storage life.

Photocatalytic oxidation (PCO), on the other hand, has been shown to have the ability to delay the adverse effects of ethylene in the storage atmosphere of fruit produce (Maneerat & Hayata, 2006; Nishizawa *et al*., 2008; de Chiara *et al*., 2015; de Chiara *et al*., 2018; Basso *et al*., 2018;

Pathak *et al*., 2019; Stroe & Rosendahl, 2019). Many authors have shown PCO to be effective in removing ethylene, but only in small scale laboratory tests. Pathak *et al*., (2017) indicated the need to do further research in real-time applications of PCO for fresh produce in storage facilities or shipping containers to provide practical data on the PCO technique. The need to extend lab-scale PCO reactor tests to lab-scale postharvest chamber tests and finally to on-site measurements was suggested by Keller *et al*., (2013). However, such tests require optimum photoreactor design scalable to industrial size, a key unresolved issue in the commercial application of PCO to ethylene degradation. The achievement of such a design requires the development of mathematical models that can be readily applied to reactor design, scale-up, and optimization (Li Puma, 2005). The central problem of scale-up of photocatalytic reactors is providing a sufficiently high specific surface area of the catalyst and the uniform illumination distribution across this area (McCullagh *et al*., 2011). The main aim of this research project was to develop a mathematical model for the effectiveness factor that accounts for the external mass transfer limitations, during photocatalytic degradation of ethylene. The model is then incorporated into the reactor design equations, demonstrating its application in reactor design and scale up. This would guide the selection of the optimum parameters for a prototype reactor suitable for installation in fruit storage containers. There is currently a gap in terms of taking successful laboratory scale projects of academic research into implementation stages applicable to industry. Thus, the project will play a vital role by contributing to the integrated postharvest ethylene management along the value chain from the farm to the consumer.

1.2 Problem Statement

PCO has shown promising results in reducing ethylene concentrations in postharvest management applications based on the laboratory scale. However, the commercial application of PCO is hindered by the lack of rigorous mathematical models required for optimum reactor design, scalable to an industrial size. This study addressed the following questions:

- Does an analytical model exist for the effectiveness factor that accounts for external mass transfer limitations?
- What is the influence of the catalyst surface morphology on the performance of the PCO reactor?
- Can the external mass transfer limitations always be ignored in the reactor design models?
- How can the developed effectiveness factor model be used to find optimum reactor design and scale-up parameters?

1.3 Research Objectives

The main aim of this study is to develop an analytical solution for the effectiveness factor that accounts for the external mass transfer limitations. Then, this model will be used to quantitatively analyze the effectiveness of the illuminated surface area of the catalysts to enable the scaling up of the PCO reactor.

The specific objectives are:

- To develop an analytical model of the effectiveness factor based on Robin boundary conditions.
- To evaluate the effect of optical thickness on the overall performance of the PCO reactor.
- To determine the rate limiting step in the overall catalytic process.
- To evaluate the effect of bulk mass transfer on the performance of the reactor.
- To develop design equations of the Damköhler number as a function of conversion for the PCO reactor.
- To compare theoretical and experimental reaction rates for ethylene photocatalysis.

1.4 Delineation

This project will not cover the following:

- PCO reactor scale up
- The construction of the prototype reactor, and its installation in fruit storage containers
- The effect of humidity on the reaction kinetics
- The effect of varying temperature on the reaction kinetics
- The effect of varying light intensity
- The treatment and analysis of fruits

1.5 Overview

This thesis presents a novel photocatalytic reactor model applied in ethylene oxidation to enable and simplify reactor scaling up.

Chapter 1 briefly introduces the study and the ethylene degradation processes. Chapter 2 details the PCO process, its application in postharvest storage on a small-scale basis, kinetic models, and mathematical modelling, and its relation to reactor scaling up. Chapter 3 details the model development process, including the analytical solution of the effectiveness factor model. This model was solved using the Robin boundary type instead of the Dirichlet boundary

type condition, introducing the Sherwood number as a new operating parameter in photocatalytic reactors. Robin boundary condition is well established in conventional reactors that do not utilize photons, but it is rarely used in solving photocatalytic reactions. Chapter 4 details the development of the reactor and its operation, catalyst preparation, experimental setup, and methodology. Chapter 5 presents and discusses the theoretical evaluation and experimental validation of the model. This involved reaction kinetics analysis and comparing the experimental reaction rate with that theoretically predicted by the model. The conclusions and recommendations from the study are outlined in Chapter 6.

CHAPTER 2
LITERATURE REVIEW

This chapter gives the basic theory of PCO and the different types of reactors used in literature which gave the basis for designing the reactor used in this study, including the catalyst types used. Ethylene reduction investigations employing PCO on small scale and their findings are discussed. Kinetic and mathematical models available in the literature are discussed.

2.1 PCO process for ethylene degradation

PCO is a method that can be used to remove/ reduce ethylene around the fruit storage atmosphere. The technique utilizes photocatalytic material, usually titanium dioxide (TiO_2), to decompose ethylene and other volatile organic compounds (VOCs) to H_2O and CO_2 under ultraviolet illumination. Figure 2.1 illustrates the basic processes involved in photocatalysis (McCullagh *et al*., 2011).

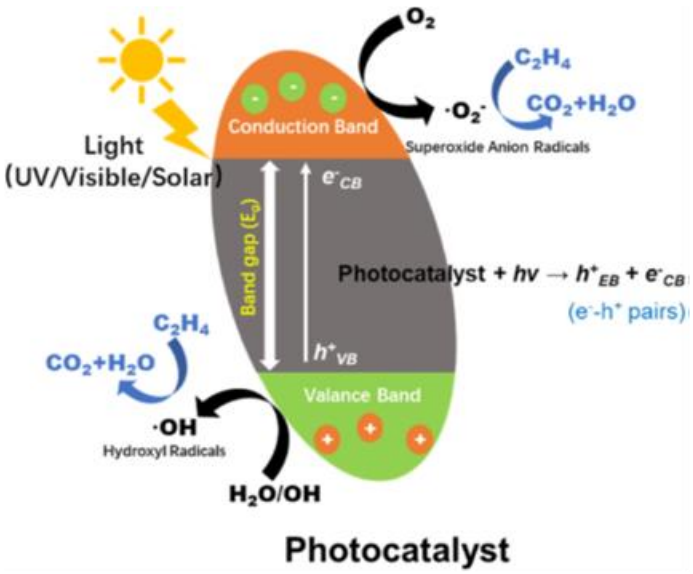

Figure 2. 1:Typical ethylene photocatalytic process over TiO_2 catalyst (Hua *et al*., 2024)

If a photon of energy greater than or equal to the band gap energy (E_g), is absorbed by the photocatalyst, an electron is promoted from the valence band to the conduction band. This generates a reducing electron (e_{CB}^-) in the conductance band and an oxidizing hole (h_{VB}^+) in the

valence band (Figure 2.1). The electrons and holes formed are highly charged and can induce redox reactions, ultimately resulting in the mineralization of pollutants. (McCullagh *et al.*, 2011).

A few studies have been conducted investigating the ability of PCO to remove ethylene in fruit storage atmosphere. Figure 2.2 shows a typical setup used in most investigations.

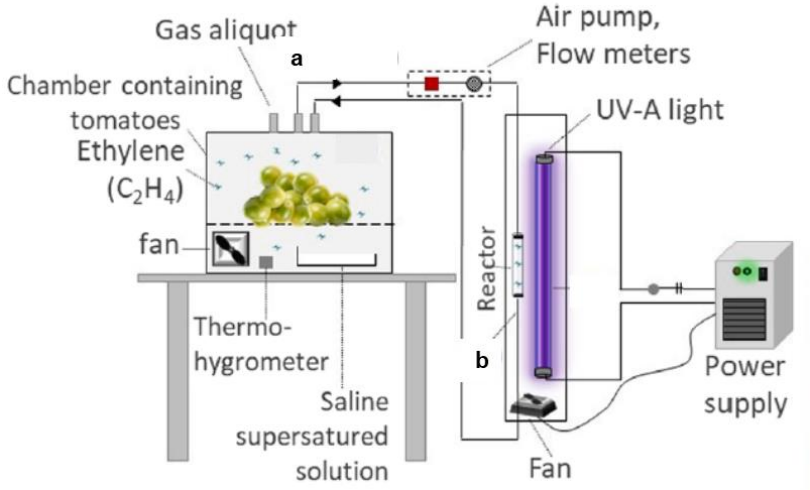

Figure 2. 2: Schematic diagram of ethylene reduction in continuous operation (a) Flow of gas to the reactor, (b) Reactor output (Adapted with permission from Fonseca *et al*., 2021)

Maneerat & Hayata, (2006) investigated the efficiency of the TiO_2 photocatalytic reaction in delaying the ripening of green tomatoes stored in a plastic box with a beaker of 100 mL TiO_2 slurry. The tests were conducted at different TiO_2 concentrations and UV-A light intensities with three tomatoes in the storage box during each test. Their results show that increasing TiO_2 concentration to 10 g/L as well as increasing the light intensity to 5 W/m^2 resulted in reduced amount of ethylene in the storage atmosphere (Maneerat & Hayata, 2006).

The authors further observed that the ripening based on the development of a full red colour occurred at 11 days for the untreated tomatoes and at 22 days for photocatalytically treated (TiO_2 concentration = 10 g/L and UV-A light intensity = 5 W/m^2) tomatoes. This observation suggests that the reduced amount of ethylene was responsible for the delayed ripening of the green tomatoes. This illustrates the potential for developing a PCO reactor/ unit that can be installed in a real-size fruit storage.

De Chiara *et al*. (2015) tested the potential of PCO in reducing the ripening trend of mature green tomatoes. Tomatoes were stored at 15 °C in two 5 L containers, and 2 ppm ethylene was continuously passed through one container for 14 days. In another container, the same concentration of ethylene was passed through via a PCO reactor (300 mL cylindrical borosilicate glass reactor with TiO_2/SiO_2 powder inside, surrounded by four black lamps as UV-A sources). It was found that the tomatoes kept in the container that was connected to a PCO reactor took a longer period to ripen, and those through which ethylene was fed directly showed a faster and more uniform ripening during the storage.

De Chiara *et al*. (2018) tested a fluidized bed photoreactor (FBP) on broccoli stored in a cold/ refrigerated room of 150 m^3 in size. The FBP consisted of a glass tubular reactor with an internal volume of 0.9 L, and Degussa P25 microparticles were used as the photocatalyst. The authors observed no significant differences in colorimetric and organoleptic parameters of whole broccoli after 12 days of storage. This is expected as the broccoli heads have a very low ethylene production rate, <0.1 μL kg^{-1} h^{-1} at 20°C (De Chiara *et al*., 2018). Though broccoli is highly sensitive to ethylene exposure, the storage of 12 days was rather too short to be conclusive. The authors concluded that the fluidized bed photoreactor prototype should be improved to make it suitable for the technological transfer of the innovation.

Basso *et al*. (2018) stored mature green cherry tomatoes in two 3.25 L cylindrical vessels (500 g of tomatoes in each vessel) at 25 °C for 5 hours. The first vessel was used as a 'control', and the second vessel was connected to the PCO reactor (a glass tube: inner diameter = 5 mm; length = 100 mm. The photocatalyst had a TiO_2 film thickness of 0.419 μm and an incident UVA irradiance of 5.18 W/m^2). Their results in Figure 2.3 show that the photocatalytic reactor maintained the ethylene concentration close to zero. The respiration rate was also found to decrease, indicating that this is an efficient technology for prolonging the shelf life of cherry tomatoes (Basso *et al*., 2018).

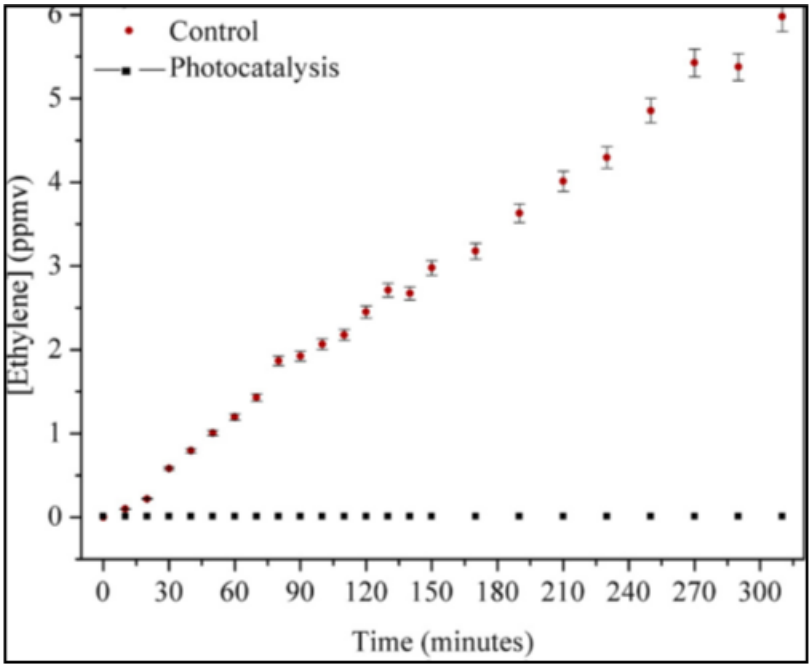

Figure 2. 3: Ethylene concentration vs time during 5 hours of cherry tomato storage at 25 °C (Adapted with permission from Basso *et al*., 2018)

Pathak *et al*. (2019) stored 6 kg of apples each in airtight chambers (190 L) housed in a walk-in cold room set at 1 °C for a duration of 8 days. One of the chambers was connected to a PCO reactor (steel reactor with the dimensions: diameter = 12 cm, height = 11 cm, consisting of three UV lamps of 3 W each, irradiating at 254 nm, and TiO_2 coated glass slides). The ethylene concentration in the PCO treated chamber was reduced from 70 μLL^{-1} to 24 μLL^{-1}, which amounts to 66% of ethylene removed.

Nishizawa *et al*. (2008) investigated the effect of PCO treatment on the quality of tomatoes by storing fifteen tomatoes each under PCO (using TiO_2 catalyst) and under normal conditions at 15°C for 17 days. The results showed that the fruit quality could be maintained during PCO treatment while keeping the ethylene levels low in closed storage systems.

Based on the available literature, it is evident that photocatalytic oxidation is an effective method for eliminating the accumulation of ethylene released by fruit inside confined spaces. However, there is still a gap in developing lab-scale tests for the large-scale reactors (scaling up) designed and optimized for use in fruit storage facilities at room temperature and possibly for other commercial applications. Mathematical modelling could be a useful tool in this regard.

2.2 Catalysts used in PCO reactors

TiO_2 in various forms is almost exclusively adopted as a key photocatalyst since it is relatively inexpensive, chemically stable, and more effective in destroying toxic contaminants (Lin *et al*., 2014). There are three polymorphic crystalline structures of TiO_2 namely, the anatase and the rutile both tetragonal, and the brookite which is orthorhombic (Etacheri *et al*., 2015; Fonseca *et al*., 2021). Anatase and rutile are the photocatalytic active phases with anatase exhibiting higher activity properties, hence in most investigations, a mixture of the two is used as the photocatalyst. As shown in Table 2.1, the most used photocatalyst with the commercial name P25 is a mixture of anatase and rutile. The band gap energy of the anatase and the rutile phases of TiO_2 is 3.2 eV and 3.0 eV respectively (Chen *et al*., 2008). Thin photocatalyst films and poorly crystallized nanoparticles are commonly associated with wider band gaps (Etacheri *et al*., 2015), which can limit photocatalytic activity. The particles deposited onto photocatalyst support materials (such as those in Figure 2.1) tend to form aggregates, causing scattering of light which then hinders light absorption by the photocatalyst, and therefore reaction efficiency (Pathak *et al*., 2017; Basso *et al*., 2018; Fonseca *et al*., 2021).

Table 2.1 shows some of the photocatalytic reactors with dimensions, the UV light sources used and the photocatalyst used. Some modifications of TiO_2 have been investigated to improve the performance of photocatalytic reactors. TiO_2 doping with metals or nonmetals is done to enable the absorption of visible light (Fonseca *et al*., 2021), while combining TiO_2 with mesoporous silica increases the surface area and pore size to enhance uniform and homogeneous dispersion of TiO_2 active sites within the structure and on the surface of the photocatalyst (De Chiara *et al*., 2015; Hussain *et al*., 2017). Photocatalytic systems suffer from drawbacks such as catalyst deactivation which results in low efficiency (Pathak *et al*., 2017). Heating the catalyst to high temperatures or exposing it to UV light at high humidity could help to recover the catalyst (Jeong *et al*., 2013).

Table 2. 1: Photocatalytic reactors using Tio_2 in various forms

Reactor Type	Light Source/ Wavelength (nm)	Catalyst(s)	Support material	Reference
Tubular borosilicate glass photo-reactor with an internal volume of 337.8 cm^3.	A black-light lamp with maximum intensity at 365 nm.	TiO_2 sol-gel	Polypropylene and glass.	Lourenço *et al*., (2017)
Steel D=12 cm, H=11 cm	3 W x 3 UV lamps, 254 nm	TiO_2 Degussa P25 based FN3 solution	Glass slides: 76 x 26 mm	Pathak *et al.,* (2019)
An aluminium duct with 10 cm × 10 cm inner cross- section area and 1.3 m length	2 UV lamps (Philips, TUV PL-S 5 W/4P), at each site of PCO filter.	Titanium dioxide	silica fibre felts modified with TiO_2 (TiO_2/SFF)	Malayeri *et al*., (2020)
Mild steel 0.66 x 0.36 x 0.36 m volume=0.086 m^3	UV LEDs 360 nm, mounted on a perforated aluminium sheet	P25, TiO_2/clay, solgel-TiO_2, N-doped TiO_2 and Bi_2O_3	wire mesh	Sharmin & Ray, (2012)
420 L-dynamic photocatalytic reactor (Closed loop stainless steel duct)	18-W UVA fluorescent tubes	P25 TiO_2	Organic fibres (cellulose, polyester and polyamide).	Batault *et al*., (2017)
Acrylic parallel piped	Five black light fluorescent lamps (300-400 nm)	TiO_2	Flat stainless steel plate (8W x8L x 0.4T cm) Corrugated SS plate (20x30x3 cm)	Passalía *et al*., (2017)
Pyrex glass (total internal volume: 1.2 L)	Osram ULTRA-VITALUX 300 W Mixture of UVA (320-400 nm and UVB (290-320 nm)	TiO_2-KIT6 KIT6 (Mesoporous silica)		Hussain *et al*., (2017))
3 L Quartz tube	Solar irradiation: 300 W tungsten lamp (315-400 nm)	Aeroxide TiO_2 P25	Pyrex glass tube	Licciulli *et al*., (2017)
300 ml cylindrical borosilicate glass (24.5 cm L, 4 cm ID)	Four black lamps UV-A: 315-400 nm	Mesoporous TiO_2/ SiO_2 nanocomposite in powder form		de Chiara *et al.,* (2015)
Pyrex glass (total volume: 2 L)	Osram ULTRA-VITALUX 300 W Mixture of UVA (320-400 nm and UVB (290-320 nm)	TiO_2 Nanoparticles (TNPs)		Hussain *et al*., (2010)

2.3 Fundamental principles of PCO

2.3.1 PCO reaction mechanism

The primary reaction mechanism for the PCO process in Figure 2.1 can be depicted as follows (Mamaghani *et al*., 2017):

$$TiO_2 + hv \rightarrow TiO_2(e^-_{CB} + h^+_{VB}) \quad (2.1)$$

$$TiO_2(h^+_{VB}) + H_2O \rightarrow TiO_2 + H^+OH^\bullet \quad (2.2)$$

$$TiO_2(h^+_{VB}) + OH^- \rightarrow TiO_2 + OH^\bullet \quad (2.3)$$

$$TiO_2(e^-_{CB}) + O_2 \rightarrow TiO_2 + O_2^{\bullet -} \quad (2.4)$$

$$2O_2^{\bullet -} + H^+ \rightarrow H_2^\bullet \quad (2.5)$$

$$HO_2^\bullet + HO_2^\bullet \rightarrow H_2O_2 + O_2 \quad (2.6)$$

$$TiO_2(e^-_{CB}) + H_2O_2 \rightarrow +OH^- + OH^\bullet \quad (2.7)$$

$$VOC + O_2 + OH^\bullet \rightarrow H_2O + CO_2 + \text{other products} \quad (2.8)$$

When the TiO_2 catalyst is exposed to UV light at wavelengths ≤ 387.5 nm, the energy (*hv*) from the photons irradiated under its surface is absorbed and causes the migration of electrons from the valence band to the conduction band (Fonseca *et al*., 2021), resulting in the formation of the electron-hole pairs (Equation 2.1). The formed valence band holes then react with water from the humid gas and adsorbed onto the catalyst to generate hydroxyl radicals (Equation 2.2). The hydroxyl radicals are also formed through the reaction of the holes with the adsorbed hydroxide (Equation 2.3). In Equation (2.4) the conductance band electrons react with electron acceptors such as oxygen which generates superoxide anion radicals (McCullagh *et al*., 2011). These radicals further interact with the adsorbed target VOC (Equation 2.8), such as ethylene molecules, leading to their decomposition to CO_2 and H_2O (Etacheri *et al*., 2015; Hua *et al*., 2024).

The final PCO of ethylene is based on equation 2.9 (Keller *et al*., 2013):

$$C_2H_4 + 3O_2 \xrightarrow{TiO_2,hv} 2CO_2 + 2H_2O \quad (2.9)$$

Understanding the photocatalysis fundamentals is of essential importance for interpreting the experimental data, analysing the parameters influencing the PCO performance, and finally, optimizing the process (Zhong & Haghighat, 2015).

2.3.2 Chemical and physical steps during PCO

In heterogeneous gas phase PCO, the mass transfer of gases from the gas stream to the solid phase catalyst plays an important role and greatly affects the reaction rate and degradation efficiency (Mamaghani *et al*., 2018). The PCO process can be divided into seven processes occurring in series, as illustrated in Figure 2.4, which can be described as follows (Zhong & Haghighat, 2015):

1) Advection (where air flows carry pollutant species),

2) Mass transfer of the reactants from the main flow to the exterior surface of the catalyst particle,

3) Molecular diffusion and/or Knudsen diffusion of the reactants from the exterior surface of the catalyst particle into the interior pore structure,

4) Adsorption of the reactant onto the interior catalyst surface,

5) Photochemical reaction on the catalyst surface,

6) Desorption of the reaction product(s) from the surface of the catalyst, and

7) Mass transfer of the products from the interior catalyst pores to the gross external surface of the catalyst by ordinary molecular diffusion and/or Knudsen diffusion, and finally, external diffusion to the main flow.

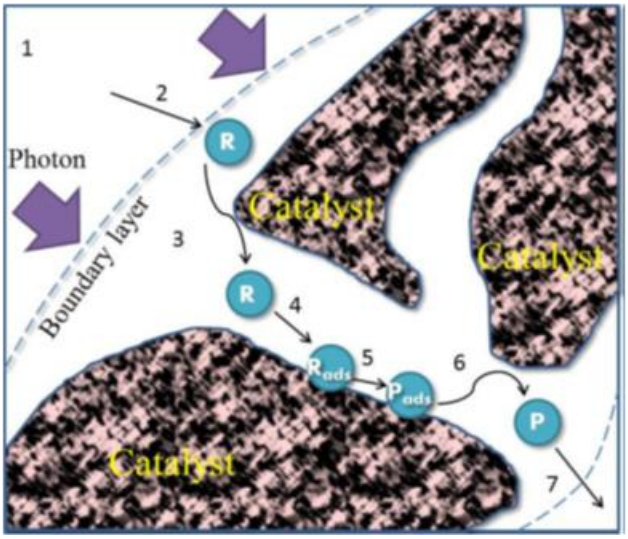

Figure 2. 4: Mass transfer processes in PCO of gases using TiO_2 (Zhong & Haghighat, 2015)

Processes 2 and 7 represent bulk mass transfer which is a function of the specific molecules, the dynamics of the flow conditions, and the geometric surface area of the catalyst (Farrauto *et al*., 2016: 20). Mass transfer correlations relating the Sherwood number to the Reynolds number and the Schmidt number are widely used to describe the interphase mass transfer steps 2-3 and 6-7 (Votruba *et al*., 1975; Yang *et al*., 2009; Zhong *et al*., 2013; Zhong & Haghighat, 2015; Malayeri *et al*., 2020). Steps 3 and 7 illustrate pore diffusion, which mainly depends on the size and shape of both the pore and the diffusing reactants and products (Farrauto *et al*., 2016: 20). Steps 4-6 are related to the chemical interactions of reactants and products (Farrauto *et al*., 2016: 20).

Understanding the above seven processes is especially important for modelling of PCO reactor as they form the basis of the mathematical equations. Any of these processes can be rate limiting and control the overall reaction rate and therefore PCO performance (Zhong & Haghighat, 2015; Farrauto *et al*., 2016: 21).

2.4 Kinetics models for PCO of ethylene

It is well established that photocatalysis experiments follow the Langmuir- Hinshelwood (L-H) model (Ye *et al*., 2010):

$$R = -\frac{dC}{dt} = \frac{k_r K_{ads} C}{1 + K_{ads} C} \tag{2.10}$$

Where R is the reaction rate (ppm.s^{-1}), C is the pollutant/ ethylene concentration (ppm), k_r is the reaction rate constant (ppm.s^{-1}) and K_{ads} is the adsorption equilibrium constant (L/mol or ppm^{-1}). Most studies on ethylene kinetics (Ye *et al*., 2010; Zhang *et al*., 2017) have neglected the term $K_{ads}C$ in the L-H model based on the assumption that the pollutant concentration is very low. This implies that $K_{ads}C \ll 1$ which then simplifies Equation (2.10) to a pseudo-first order reaction rate:

$$-\frac{dC}{dt} = K_r K_{ads} C = K_{app} C \tag{2.11}$$

Where, $K_{app} = k_r K_{ads}$ is the apparent pseudo-first order kinetic constant. If C_0 is the initial concentration and t is the reaction time, the integrated form of Equation (2.11) may be written as:

$$ln\left(\frac{C}{C_0}\right) = K_{app}.t \quad (2.12)$$

K_{app} is then evaluated by plotting $ln(C/C_0)$ against the reaction time and is given by the slope of the obtained straight line.

Zhang *et al*. (2017) used the rate constant to describe the decomposition efficiency of ethylene in their investigation of five different photocatalytic composite materials (titanium dioxide nanotube arrays with silver and reduced graphene oxide). K_{app} was obtained using Equation (2.12) and varied from 1.89 x 10^{-4} to 3.90 x 10^{-4} min^{-1} for the five photocatalytic materials tested. Linear regression was used to fit the data obtained with R^2 in the range 0998 – 0.999 for the different photocatalyst materials.

Licciulli *et al*. (2017) also used Equation (2.12), assuming the first order reaction to determine the rate constant for ethylene PCO under solar irradiation. K_{app} values obtained are 1.96 x 10^{-3} min^{-1} and 2.68 x 10^{-3} min^{-1} for TiO_2 (P25) and $CuPcTiO_2$ (copper phthalocyanine sensitized TiO_2) respectively when coated on glass tubes.

Song *et al*. (2018) used K_{app} from the pseudo-first order model to compare the performance of different TiO_2 (P25)/Bi_2WO_6 nanocomposite photocatalysts in degrading ethylene under visible light. The calculated values of K_{app} ranged from 1.148 x 10^{-4} for pure TiO_2 (P25) to 9.081 x 10^{-4} for 35% TiO2 (P25)/Bi_2WO_6.

Maneerat & Hayata (2008) obtained K_{app} values ranging from 5.6 x10^{-3} to 1.5 x10^{-1} h^{-1} for PCO degradation in TiO_2 coated packages in the range 0.1% – 10% TiO_2 respectively.

Stroe & Rosendahl (2019) used a photocatalytic batch reactor to assess the kinetics of the oxidation of ethylene over immobilized titanium dioxide and the effect of initial pollutant concentration on the kinetics using the L-H kinetic model. In this study, a comparison was done between the direct solution of the L-H model, the reduced L-H model to pseudo-first order reaction rate as well as the integrated and linearized L-H model Equation (2.13). The study found that the use of the simplified first order model resulted in a deviation from the experimental data. This is in contrast with most studies in which the first order was found to fit

the experimental data well. Reactor conditions such as the control of constant temperature during the kinetic experiments and the type of light source influence the kinetic experimental results. In Stroe & Rosendahl's (2019) study, LED's emitting wavelength between 340 nm and 400 nm (with a maximum peak of 365 nm) were used. The proven wavelength to initiate an adequate reaction in ethylene photocatalysis is 254 nm. The treatment of the two kinetic constants as one single term is a drawback as a value for each constant cannot be determined unless ethylene adsorption isotherms are investigated to obtain a value for K_{ads} (Stroe & Rosendahl, 2019). Thus, there is a need to investigate the suitability of the simplified model for the kinetic analysis of ethylene PCO. The first step for this investigation would be the determination of the true reaction order to confirm the correctness of the popular first order assumption. The direct solution of the L-H model failed to predict the initial concentration; however, the final concentration could be estimated with less deviation compared to the first order model. Lambert W-function was used to solve Equation (2.13) for concentration, C, as an explicit solution cannot be found.

$$\frac{1}{k_r K_{ads}} ln\left(\frac{C_0}{C}\right) + \frac{1}{k_r}(C_0 - C) = -t \tag{2.13}$$

This model was found to best fit the experimental data although there were constraints in obtaining the numerical solution, hence the use of the Lambert W-function which is time consuming.

Basso *et al*., (2018) evaluated k_r and K_{ads} by plotting the reciprocal of the reaction rate (*1/R*) versus the reciprocal of ethylene concentration (*1/C*), following the linear form of the L-H model Equation (2.14) and *R* was calculated by Equation (2.15) from the slope of the plot of *X* versus *F/A*.

$$\frac{1}{R} = \frac{1}{k_r} + \frac{1}{k_r K_{ads} C} \tag{2.14}$$

$$R = X.C.\frac{F}{A} \tag{2.15}$$

Where *X* is the conversion of ethylene, *F* is the gas flow rate and *A* is the catalyst area. The L-H model was found to well describe the linear dependence of ethylene concentration on the reaction rate, although this achievement was only possible at high flow rates to ignore the

mass transfer limitations. The calculated parameters are k_r = 0.6694 nmolm^{-2} h^{-1} and K_{ads} = 1.66 nm^3 mol^{-1}. This is a similar approach described by Einaga *et al*., (2015), although, in their study, *R* was calculated by Equation (2.16) in which W (catalyst weight) was used instead of A in Equation (2.15). The estimated kinetic parameters are k_r = 1.30±0.03 x10^{-2} mols^{-1}m^{-2} and K_{ads} = 4.8±0.4 x10^5 Lmol^{-1}. The approach is based on the assumption that the photoreactor is a plug-flow reactor in which no fluid mixing and back mixing occur.

$$R = X.C.\frac{F}{W} \tag{2.16}$$

Sirisuk *et al*., (1999) did preliminary studies for PCO of ethylene in a continuous tubular photoreactor packed with titania coated glass rings. The L-H rate expression was substituted into the design equation for a plug flow reactor, resulting in the equation:

$$\frac{W}{F} = \frac{1}{k_r K_{ads} C_0} ln\left(\frac{C_0}{C}\right) + \frac{1}{k_r}\left(\frac{C_0 - C}{C_0}\right) \tag{2.17}$$

Equation (2.17) may be written in different forms to determine the kinetic parameters:

$$\frac{WC_0/F}{(C - C_0)} = -\frac{1}{k_r} - \frac{1}{k_r K_{ads}} . \frac{ln(C/C_0)}{(C - C_0)} \tag{2.18}$$

Where W is the weight of the catalyst and F is the molar flow rate of ethylene. The kinetic parameters (k_r = 4.27 x 10^{-9} mol/g.s, K_{ads} = 4.95 x 10^4 L/mol) were obtained from linear regression analysis of Equation (2.18). These were used to predict the conversions at different *W/F* ratios and the model was found to provide a good fit of the data.

In a study by Zorn *et al*., (2000) the half order model provided a slightly better fit to the data compared to the L-H model. A linearized half order model was used to calculate the kinetic rate constants (Zorn *et al*., 2000):

$$C^{1/2} = C_0^{1/2} - k_r \frac{Wt}{2V_{res}} \tag{2.19}$$

Where V_{res} is the reservoir volume (L). The data was fit by performing the least-squares regression analyses of the plot $C^{1/2}$ versus *t*, where the reaction rate constant is the negative slope multiplied by $2V_{res}/W$ (Zorn *et al*., 2000). The calculated reaction rate constants in

$mol^{1/2}L^{1/2}\ g^{-1}s^{-1}$ for an unplatinized TiO_2/ZrO_2 thin film catalyst are 1.8 x 10^{-4}, 3.22 x 10^{-4} and 3.34 x 10^{-4} at 30°C, 70°C and 107°C respectively: 1.67 x 10^{-4}, 3.35 x 10^{-4} and 6.62 x 10^{-4} for platinized TiO_2/ZrO_2 at 30°C, 70°C and 107°C respectively.

In all the models discussed above, the effects of humidity, oxygen, carbon dioxide (CO_2), temperature, and light intensity on ethylene degradation rate are ignored. The reaction rate generally increased with increasing initial inlet ethylene concentration. Obee & Hay (1997) employed a temperature dependent rate that takes into account the effect of water, but also ignored CO_2 assuming that it did not influence the observed rates and that only ethylene and water vapour were important. The temperature dependent rate model is given by:

$$R = \frac{k_o^{'}\, exp(-E/RT)\, K'_E \frac{exp(-\Delta H_E/RT)}{\sqrt{T}} X_E}{1 + K'_E \frac{exp(-\Delta H_E/RT)}{\sqrt{T}} X_E + K'_W \frac{exp(-\Delta H_W/RT)}{\sqrt{T}} X_W} \tag{2.20}$$

A model by Lin *et al*., (2014) accounts for all the possible effects except CO_2 which was assumed to not influence the reaction rate:

$$R = I^{\alpha} k' exp\left(-\frac{E_a}{RT}\right) \frac{K'_E\, exp\left(\frac{-\Delta H_E/RT}{\sqrt{T}}\right) C_E}{1 + K'_E\, exp\left(\frac{-\Delta H_E/RT}{\sqrt{T}}\right) C_E + K_W\, exp\left(\frac{-\Delta H_W/RT}{\sqrt{T}}\right) C_W} \left(\frac{K'_{O_2}\, exp\left(\frac{-\Delta H_{O_2}/RT}{\sqrt{T}}\right) C_{O_2}}{1 + K'_{O_2}\, exp\left(\frac{-\Delta H_{O_2}/RT}{\sqrt{T}}\right) C_{O_2}} \right) \tag{2.21}$$

It was found that the PCO rate increased with increasing concentrations of ethylene and oxygen, light intensity, and temperature (30°C and 45°C), but decreased with increasing water vapour concentration (humidity). The decrease in degradation efficiency with increasing humidity content was also observed by Tytgat *et al*. (2012).

The rate law by Yamazaki *et al*., (1999) incorporates concentrations of ethylene, water vapour, and oxygen as well as the light intensity:

$$R = -\frac{d[C_2H_4]}{dt} = \frac{k_9 K_8 I_a \varphi K_{C_2H_4}}{k_{OH}\left(1 + K_{C_2H_4} P_{C_2H_4} + K_{H_2O} P_{H_2O}\right)} \times \frac{K_{O_2} P_{O_2}}{1 + K_{O_2} P_{O_2}} \tag{2.22}$$

The rate constant values available in the literature are not comparable since different types of photocatalysts (including different sources of the commonly used TiO_2) have been employed, which exhibit different photocatalytic activities. The differences in photocatalytic activities can

be qualitatively attributed to differences in morphology, crystal phase, specific surface area, particle aggregate size, and surface density of OH groups in the TiO_2 samples (Mills & Le Hunte, 1997). Thus, for comparable results, it is important to use a standard form of TiO_2 such as P25, however, this has been used in different forms (powder, thin films, mixed/ doped with other compounds/ metals) and formulations. Therefore, a standardized catalyst preparation method is also necessary for the results to be comparable. In the case of thin films, which are of popular interest due to their ease of handling, the true reaction rate is also influenced by the thickness of the film. This is due to the possible diffusion limitations as well as the transport of photons. Even with the same deposition method, the properties of the film may change very much if the preparative conditions vary only slightly (Camera-Roda & Santarelli, 2007). Most reported kinetic parameters in the literature strongly depend on the experimental conditions and cannot be easily extrapolated to other conditions (Malayeri *et al*., 2021). None of the kinetic models in the literature have considered the possibility and consequently the influence of mass transfer resistance. It is also worthwhile to note that the kinetic model varies with operating conditions or reactor designs (Malayeri *et al*., 2019).

2.5 Mathematical modelling of PCO reactors and scaling up

The traditional scaling up procedure involves laboratory experiments in which the proposed reactor is gradually increased to the desired commercial size (Satuf *et al*., 2007). This means that several reactors must be built, making this approach expensive as well as time consuming. Scaling up procedures employing mathematical models (Satuf *et al*., 2007) can be cost effective and less time consuming. These mathematical models can be instrumental in determining the effectiveness factor, a key parameter in quantitative analysis of the factors that determine the effective utilization of the illuminated surface area of the catalyst. Currently, no mathematical models in the literature define the effectiveness factor for ethylene PCO. Furthermore, very limited studies are reported on mathematical models coupling advection, diffusion, and the reaction rate expression in the overall mass balance. This is a key model required in developing the effectiveness factor equation.

A model by Nielsen *et al*., (2015) for ethylene PCO is based on simple Langmuir– Hinshelwood adsorption kinetics and the advection and diffusion of gas through the porous photocatalyst. Figure 2.5 shows the schematic diagram of the photocatalyst coordinate system.

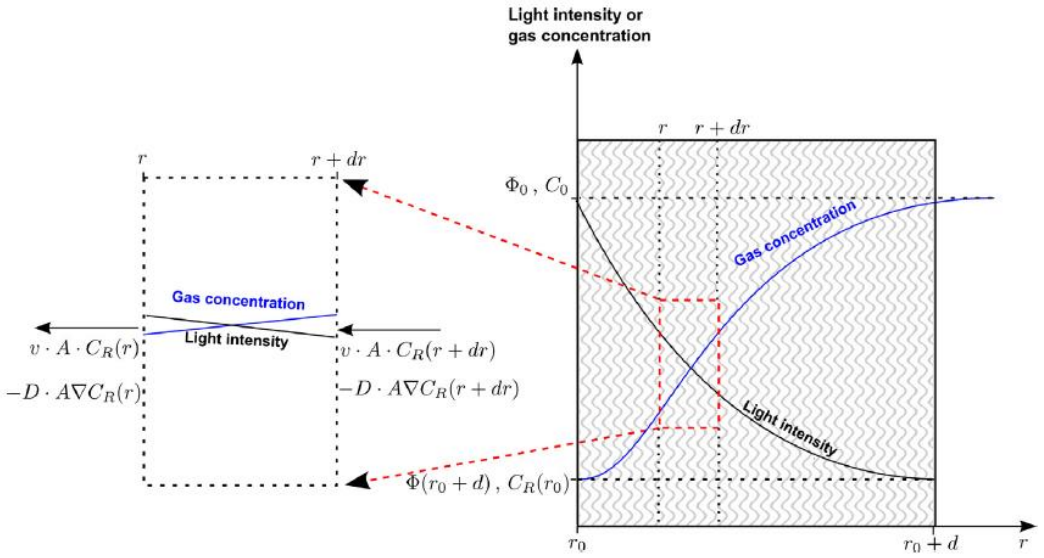

Figure 2. 5: Schematic cross-section view of TiO_2 impregnated quartz wool photocatalyst (Adapted with permission from Nielsen *et al.*, 2015)

The governing equation for their model in cylindrical coordinates shown in Figure 2.5 is:

$$0 = D\frac{d^2C_R}{dr^2} + D\frac{1}{r}\frac{dC_R}{dr} \pm |v_0|\frac{r_0}{r}\frac{dC_R}{dr} - \gamma\theta_R(C_R)\frac{r_0}{r}exp(-\alpha[r - r_0]) \tag{2.23}$$

And, the simplified governing equation for quasi one dimensional geometry is:

$$0 = D\frac{d^2C_R}{dx^2} \pm |v_0|\frac{dC_R}{dx} - \gamma\theta_R(C_R)\,exp(-\alpha x) \tag{2.24}$$

In Equations (2.23) and (2.24), r is the radial coordinate, r_0 is a reference radial distance, α is the average absorption coefficient, γ is a net rate constant (a combination of the magnitude of the light intensity at the reference position, the amount of catalyst area per unit volume and the rate constant), θ_R is the fractional surface coverage of reactant, $|v_0|$ is the magnitude of the gas velocity at r_0 (the sign in front of the velocity magnitude depends on the direction of the gas flow), D is the diffusivity, C_R is the reactant concentration and x is the position measured from the illuminated surface.

The assumptions in the model include steady state, radial flow, that the photocatalyst sheet is isothermal, and that the gas is incompressible. With this model, the geometrical photocatalyst area required to reduce ethylene in a full container's shipment could be estimated but only at high gas velocity. The authors noted that with the limit of high flow velocity, the total

photooxidation rate was independent of the flow velocity. This is to be expected because the mass transfer limitations are eliminated at high gas flow rates. However, operating at high flow rates is not always technically possible and can lead to such short residence time that the inlet and outlet concentrations may not be significantly different (Biard *et al*., 2007). Furthermore, it is not clear in the model how the radiation distribution was characterized, as this is one of the important factors in the photocatalytic reactor, which directly impacts the activity of the catalyst.

Li Puma (2005) did an analysis of steady-state continuous flow slurry photocatalytic reactors for water purification by TiO_2 photocatalysis. The developed dimensionless mathematical models can be easily used for scale-up and design of photocatalytic reactors of different geometries irradiated by UV lamps or solar radiation (Li Puma, 2005). Although no evaluation of η was done in this study, the mathematical models can be further developed for the determination of this important parameter. A rigorous mathematical model should incorporate the reaction kinetic model, the light irradiance field model, and the mass transport model and be capable of evaluating the limitations such as the mass transfer, surface reaction, and photon transfer/ distribution. No studies of such a model have been found for the photocatalytic oxidation of ethylene.

The photocatalyst is deposited as a thin film on support materials such as glass, stainless steel sheets, and fibres in photocatalytic processes. One of the advantages of immobilizing TiO_2 photocatalyst is that it results in a porous catalyst layer, providing a larger surface area for the degradation of the pollutant (Chen *et al*., 2000). However, this thin catalyst film is usually subjected to mass transfer as well as photon absorption limitations. A good indication of the extent to which mass and photon transport limitations affect the immobilized photocatalytic layer is given by the effectiveness factor (Parrino *et al*., 2019).

The effectiveness factor (η) is the ratio of the actual reaction rate to the theoretical reaction rate if the whole surface area of the catalyst is available to the bulk concentration of the pollutant (Fogler, 2020: 1528). It may be written as (Hill & Root, 2014: 380):

$$\eta = \frac{Actual\ rate\ for\ the\ entire\ catalyst}{Rate\ evaluated\ at\ external\ surface\ conditions} \tag{2.25}$$

It is a dimensionless number that measures how effectively the catalyst is being used (Rawlings & Ekerdt, 2002: 371) to facilitate a reaction. For η near unity, the process is mass-transfer controlled (i.e., the reactant can diffuse quickly through the catalyst), and for η near

zero, the process is controlled by surface reaction (i.e., the mass transfer limitations prevail). An additional factor to consider in photocatalytic reactions is the absorption of light, as this directly impacts the activity of the catalyst.

A few models found in the literature that evaluated this parameter in photocatalytic reactions have focused only on the internal effectiveness factor, which considers diffusion inside the catalyst layer (Edwards *et al*., 1996; Camera-Roda & Santarelli, 2007). Edwards *et al*., (1996) used the orthogonal collocation method to determine the effectiveness factor numerically for photocatalytic reactions obeying zero order, first order, second order, and generalized Langmuir-Hinshelwood/ Hougen-Watson kinetics. In their analysis, the convective mass transfer has been neglected based on the assumption that the polluted mixtures are sufficiently dilute. Based on the conclusions by the authors, the models, and the plots of effectiveness factor vs. Thiele modulus presented may be applicable in the design of photocatalytic reactors, to account for varying concentrations and photon-flux levels within the catalyst film, thus, excluding the concentration profiles through the external film layer. Thiele modulus is the ratio of internal diffusion to the reaction rate. Figure 2.6 below shows the plots of effectiveness factor versus Thiele modulus at different optical film thicknesses for a reaction which obeys a first-order rate expression.

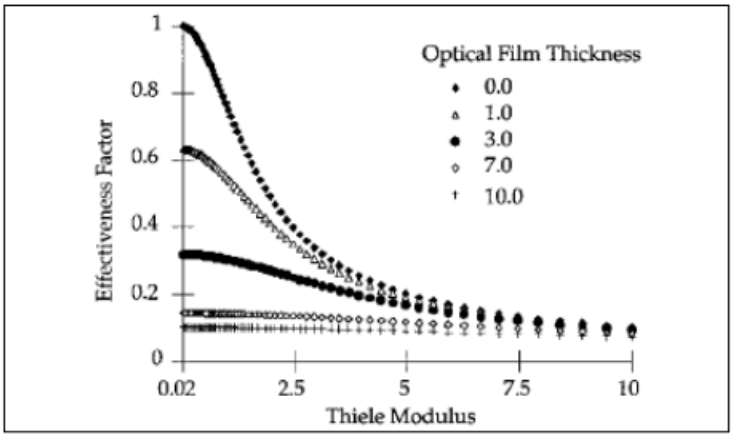

Figure 2. 6: Effectiveness factor vs. Thiele modulus (Adapted with permission from Edwards *et al*., 1996)

Camera-Roda & Santarelli (2007) used the numerical solution by control volume method to determine the effectiveness factor in their study to investigate the optimum photocatalytic film thickness for application in the treatment of contaminants in water. One of the boundary

conditions employed in their mathematical model is that of fixed concentration at the fluid–film interface, ignoring the concentration profile through the catalyst's external film layer. A semi-log plot of the effectiveness factor vs. α (the definition of this parameter in this paper is similar to the Thiele Modulus) at different values of the optical thickness is depicted in Figure 2.7. The plots of interest in Figure 2.7 are the solid lines representing the photocatalyst illuminated at the catalyst film side. Figure 2.7 shows that the photocatalytic degradation process is controlled by internal diffusion when α, is high and by the transport of photons when the optical thickness is high.

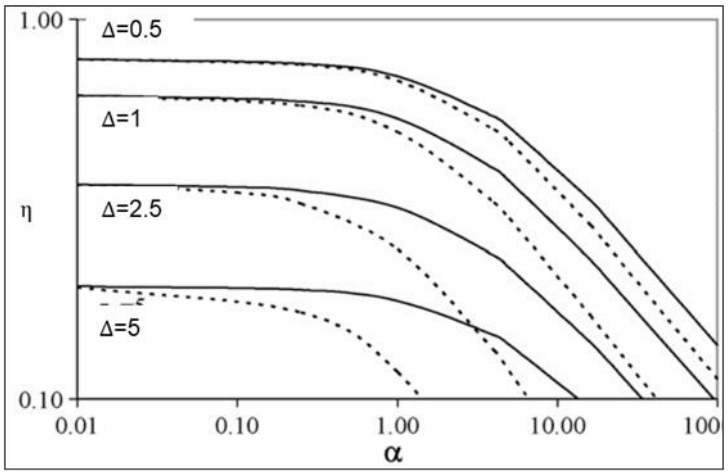

Figure 2. 7: Effectiveness factor vs α at different values of Δ (Adapted with permission from Camera-Roda & Santarelli, 2007)

To optimize and scale up the PCO reactor plots of the type in Figures 2.6 and 2.7 need to be developed and validated experimentally for ethylene. It is a great tool for analysing the effect of parameters such as the catalyst thickness and the photon absorption, which play a crucial role regarding the activity of the catalyst and, consequently, the reaction rate. Studies of this type that account for external diffusion limitations and for ethylene photocatalysis are currently not available.

An analytical solution for immobilized photocatalytic microreactors was presented by Visan *et al.*, (2014). The model is said to include species transport in the flow channel governed by advection and diffusion; however, convection through the film layer is not explicit in their equation (2.26) for the internal effectiveness factor. In this study, equation 2.26 was redeveloped and extended to include the effect of the external mass transfer limitations.

$$\eta=\frac{1}{\phi}\frac{I_1\left(\frac{2\phi\sqrt{e^{\gamma\alpha\delta}}}{\gamma\alpha\delta}\right)K_1\left(\frac{2\phi}{\gamma\alpha\delta}\right)-K_1\left(\frac{2\phi\sqrt{e^{\gamma\alpha\delta}}}{\gamma\alpha\delta}\right)I_1\left(\frac{2\phi}{\gamma\alpha\delta}\right)}{I_0\left(\frac{2\phi}{\gamma\alpha\delta}\right)K_1\left(\frac{2\phi\sqrt{e^{\gamma\alpha\delta}}}{\gamma\alpha\delta}\right)+K_0\left(\frac{2\phi}{\gamma\alpha\delta}\right)I_1\left(\frac{2\phi\sqrt{e^{\gamma\alpha\delta}}}{\gamma\alpha\delta}\right)} \quad (2.26)$$

Other authors simply used the effectiveness factor, Equation (2.27) for a straight cylindrical pore (Levenspiel, 1999; Hill & Root, 2014).

$$\eta=\frac{\tanh\phi}{\phi} \quad (2.27)$$

Dijkstra *et al*., (2002) used the equation to evaluate internal diffusion limitations in the immobilized catalyst for the photocatalytic degradation of formic acid. Krivec *et al*., (2015) used the equation to account for pore diffusional effects in the photocatalytic degradation of phenol in a fixed TiO_2 microreactor. Murshed *et al*., (2022) adopted the effectiveness factor equation (2.28) by Fogler (2020: 1530) to evaluate the internal mass transfer effects on the photodegradation of Astrazon Orange G (AOG) dye in spherical ZnO photocatalyst.

$$\eta=\frac{3}{\phi^2}(\phi\coth\phi-1) \quad (2.28)$$

It is worth noting that equations 2.27 and 2.28 were developed for conventional reactors and may not apply to photocatalytic reactors as they do not consider the UV light intensity. The major limitation of the available effectiveness factor models for photocatalytic reactors is that they are developed based on the Dirichlet boundary type condition (Edwards *et al*., 1996; Camera-Roda & Santarelli, 2007; Visan *et al*., 2014). In this boundary condition, an assumption is that the bulk pollutant concentration is the same as the concentration at the catalyst surface, or that there is no external mass transfer resistance. This is not always true because of the species concentration gradient through the film layer. If the external mass transfer rate is low, the concentration in the bulk fluid and that at the external catalyst surface are significantly different (Rawlings & Ekerdt, 2002: 385). Thus, the external mass transfer limitations which incorporate convection and diffusion of species in the film layer should be considered. Equation (2.29) by Rawlings & Ekerdt, (2002: 386). was developed based on the Robin boundary

condition for first order reaction in a spherical catalyst, however, it is also for conventional reactors not utilizing photon.

$$\eta=\frac{1}{\phi}\left[\frac{1/\tanh 3\phi - 1/(3\phi)}{1+\phi(1/\tanh 3\phi - 1/(3\phi))/B}\right] \quad (2.29)$$

Where *B* is the Biot number defined as the ratio of external mass transfer coefficient to internal diffusion.

This literature review revealed that extensive research has been conducted on the reduction of ethylene using different types of PCO reactors and fruit storage on a small scale. TiO_2 is the main photocatalyst used in different forms as powder particles, solutions, and thin, coated films. These reactors were found to reduce ethylene and extend the storage duration of tomatoes (Maneerat & Hayata, 2006, Nishizawa *et al*. 2008, De Chiara *et al*. 2015, Basso *et al*. 2018) and apples (Pathak *et al*. 2019). These findings brought confidence in the use of the PCO technique and probed research interest in methodologies that may aid in scaling up. Mathematical models are usually the first step toward developing such methodologies and in heterogeneous catalysis, the effectiveness factor is a key parameter that facilitates quantitative analysis of how effective the illuminated catalyst is utilised. This literature review revealed that although limited effectiveness factor models for photocatalytic reactors are available, these models do not consider cases where there are limitations in terms of mass transfer from the gas stream to the catalyst (Edwards *et al*., 1996; Camera-Roda & Santarelli, 2007, Visan *et al*., 2014); others are for conventional catalytic reactors not utilizing UV light (Levenspiel, 1999; Rawlings & Ekerdt, 2002: 385; Hill & Root, 2014; Fogler 2020). This study will address this gap by developing the effectiveness factor model that incorporates both convection and diffusion and validating it experimentally using ethylene as the model pollutant.

CHAPTER 3

MODEL DEVELOPMENT

This chapter describes the basis of the model, including the assumptions and the governing equations leading to the main equation to be solved (the model) in this work. The step-by-step solution of the model effectiveness factor is detailed. For a quick estimation of the effectiveness factor, an approximation of the main model is also developed in this chapter.

3.1 Model Description and Assumptions

The photocatalytic reactor considered in this study is a continuous flow reactor utilizing a thin film of TiO_2 photocatalyst immobilized onto a porous nonwoven vilene and UV light as a source of photons. The basis of the model is depicted in Figure 3.1(b), where x = 0 represents the position (m) at the catalyst surface, $x = \delta$ is the catalyst layer thickness (m) and L is the macroscopic length of the catalyst support (m). C_{Ab} is the concentration of the gas pollutant in the bulk and C_A (mol/m^3) is the concentration profile through the gas film layer. Figure 4.1(c) shows the pores within the TiO_2 film assumed to be straight cylindrical with radius r.

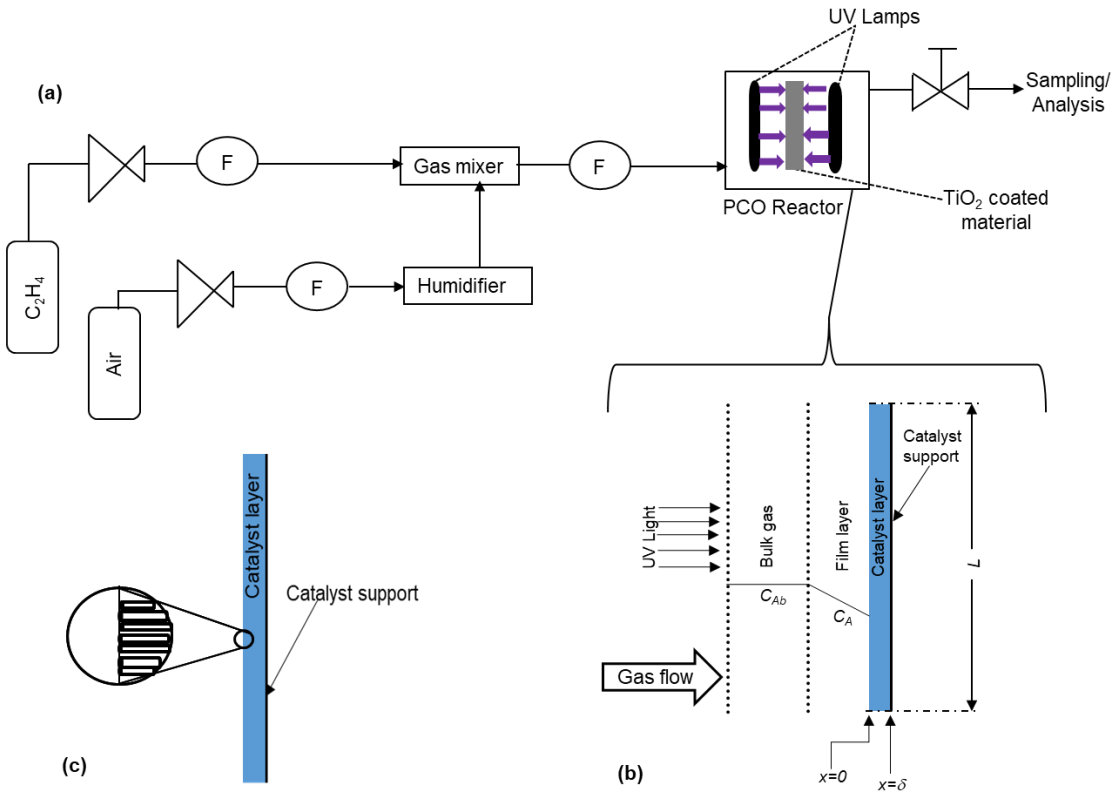

Figure 3. 1: (a) Flow diagram of the photocatalytic reactor process; (b) schematic of the concentration profile in the immobilized photocatalytic system (Adapted with permission from Edwards *et al.*, 1996) ; (c) TiO_2 pores within the catalyst layer

The model will be based on the following operating conditions and assumptions: (1) the flow is steady and one-dimensional in the *x* direction; (2) the system is isothermal; (3) the diffusion coefficient (D_{AB}) is constant; (4) the reaction follows pseudo first order kinetics; and (5) the light intensity can be modelled using Beer Lambert's law. The purpose of the model is to determine a mathematical solution for the concentration profile through the photocatalyst that incorporates the change in concentration through the gas film layer. This concentration profile is then incorporated into the equation for calculating the effectiveness factor.

3.2 Governing Equations

The catalyst layer in Figure 3.1(b) can be represented in rectangular coordinates as shown in Figure 3.2.

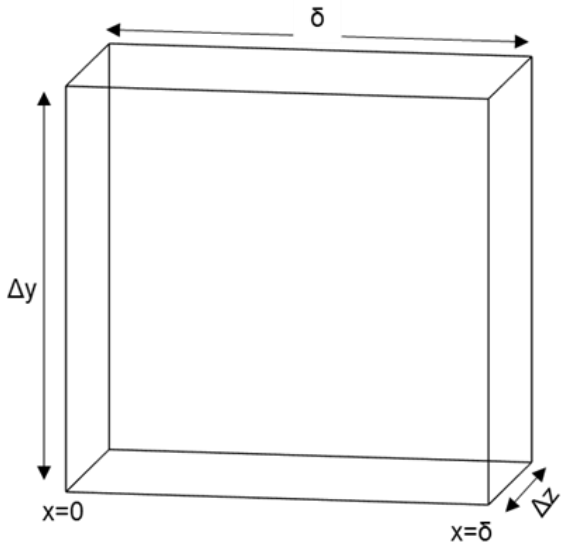

Figure 3. 2: Representation of the catalyst layer

The mass balance in the x direction is given by:

$$\frac{\mathrm{d}}{\mathrm{dt}}(\rho\Delta\mathrm{x}\Delta\mathrm{y}\Delta\mathrm{z}) = \left(\mathrm{J}_{A,x|\mathrm{x}} - \mathrm{J}_{A,x|\mathrm{x}+\Delta\mathrm{x}}\right)\Delta\mathrm{y}\Delta\mathrm{z} - \mathrm{r}_{\mathrm{A}}(\Delta\mathrm{x}\Delta\mathrm{y}\Delta\mathrm{z}) \tag{3.1}$$

Where $\mathrm{J}_{\mathrm{A,x}}$ is the diffusion flux of species A. Applying the steady state flow assumption and dividing through by $\Delta\mathrm{x}\Delta\mathrm{y}\Delta\mathrm{z}$ gives:

$$0 = \frac{\left(\mathrm{J}_{A,x|\mathrm{x}} - \mathrm{J}_{A,x|\mathrm{x}+\Delta\mathrm{x}}\right)}{\Delta x} - \mathrm{r}_{\mathrm{A}} \tag{3.2}$$

The term $\mathrm{J}_{\mathrm{A},x|\mathrm{x}+\Delta\mathrm{x}}$ can be written as:

$$\mathrm{J}_{A,x|\mathrm{x}+\Delta\mathrm{x}} = \mathrm{J}_{A,x|\mathrm{x}} + \Delta\mathrm{x}\frac{\mathrm{dJ}_{A,x}}{\mathrm{dx}} \tag{3.3}$$

The diffusion flux is given by Fick's law:

$$\mathrm{J}_{A,x} = -D_{AB}\frac{\mathrm{dC}_A}{\mathrm{dx}} \tag{3.4}$$

Substituting Equations (3.3) and (3.4) into Equation (3.2) gives:

$$\mathrm{D}_{\mathrm{AB}}\frac{\mathrm{d}^2\mathrm{C}_A}{\mathrm{dx}^2} = \mathrm{r}_{\mathrm{A}} \tag{3.5}$$

The reaction rate, r_A, in Equation (3.5) is based on the unit reaction volume. As depicted in Figure 3.1(b), the reaction of interest is a heterogeneous gas-solid type which is dependent on the catalyst surface area. It is therefore necessary to redefine the reaction rate in terms of the unit surface area of the catalyst using the following relation:

$$\dot{r}_A\mathrm{A}_s = \mathrm{r}_{\mathrm{A}}\mathrm{V}_R \tag{3.6}$$

Where $\mathrm{A}_{\mathrm{s}}=2\mathrm{Lz}$ is the catalyst surface area, $\mathrm{V}_{\mathrm{R}}=\mathrm{Lz}\bar{\mathrm{r}}$ is the reaction volume and $\dot{r}_A$ is the reaction rate per unit irradiated surface area of the photocatalyst. Rearranging Equation (3.6) and substituting the definitions of A_s and V_R gives:

$$\mathrm{r}_{\mathrm{A}} = \dot{\mathrm{r}}_{\mathrm{A}}\left(\frac{2\mathrm{Lz}}{\mathrm{Lz}\bar{\mathrm{r}}}\right) = \dot{\mathrm{r}}_{\mathrm{A}}\left(\frac{2}{\bar{\mathrm{r}}}\right) \tag{3.7}$$

Substituting Equation (3.7) into Equation (3.5) results in the diffusion-reaction equation:

$$\mathrm{D}_{\mathrm{AB}}\frac{\mathrm{d}^2\mathrm{C}_{\mathrm{A}}}{\mathrm{dx}^2} = \dot{\mathrm{r}}_{\mathrm{A}}\left(\frac{2}{\bar{\mathrm{r}}}\right) \tag{3.8}$$

Equation (3.8) may be nondimensionalized by introducing the dimensionless variables:

$$C=\frac{C_A}{C_{A0}};\qquad X=\frac{x}{\delta};\qquad R=\frac{\dot{r}_A}{r_0}$$

where r_0 is the reaction rate per unit area evaluated at the surface of the catalyst. Substituting the dimensionless variables into Equation (3.8) and rearranging gives:

$$\frac{d^2C}{dX^2}=\left(\frac{2\delta^2}{C_{A0}D_{AB}\bar{r}}\right)\dot{r}_A \tag{3.9}$$

By further assuming that the efficiency of photons conversion to an oxidizing hole is constant, the reaction rate for ethylene PCO has been proven to be directly proportional to the light intensity (Yamazaki *et al.*, 1999). Therefore, the reaction rate for reactions following the Langmuir-Hinshelwood (L-H) model can be written as:

$$\dot{r}_A=k_r I\frac{K_{ads}C_A}{1+K_{ads}C_A} \tag{3.10}$$

Where k_r and I are the reaction rate constant and the UV light intensity respectively. The Beer-Lambert law is widely used to model UV light intensity:

$$I=I_v e^{-\mu x} \tag{3.11}$$

Where I_v is the intensity of the UV light entering the catalyst layer and μ is the light absorption coefficient for UV in the catalyst. Combining equations (3.9), (3.10), and (3.11), and applying dimensional analysis gives:

$$\frac{d^2C}{dX^2}=\left[\left(\frac{2\delta^2 I_v k_r}{D_{AB}\bar{r}}\right)\left(\frac{1}{\frac{1}{C_{A0}K_{ads}C}+1}\right)\right]e^{-\Delta X} \tag{3.12}$$

where $\Delta = \mu\delta$ is the dimensionless optical thickness. For the first order approximation stated in the assumptions (i.e., if $1/C_{A0}K_{ads}$ >> 1), the equation becomes:

$$\frac{d^2C}{dX^2}=\phi^2 C e^{-\Delta X} \tag{3.13}$$

where ϕ^2 is the Thiele modulus defined as:

$$\phi^2 = \frac{2\delta^2 l_v k_r}{D_{AB}\bar{r}} \tag{3.14}$$

For Equation (3.13) to be solved analytically, it must be transformed to the modified Bessel's equation which has a known solution. To do this, from Equation (3.13), the following steps are done:

Let; $$y = e^{-\Delta X} \tag{3.15}$$

Then, differentiating y with respect to X gives:

$$\frac{dy}{dX} = -\Delta e^{-\Delta X} \tag{3.16}$$

The derivative dC/dX in Equation (3.13) may be written as:

$$\frac{dC}{dX} = \frac{dy}{dX}\frac{dC}{dy} \tag{3.17}$$

Substituting Equation (3.16) into Equation (3.17) gives:

$$\frac{dC}{dX} = -\Delta e^{-\Delta X}\frac{dC}{dy} \tag{3.18}$$

Therefore;

$$\frac{d^2C}{dX^2} = \frac{d}{dX}\left(-\Delta e^{-\Delta X}\frac{dC}{dy}\right) \tag{3.19}$$

Differentiating the right-hand side of Equation (3.19) using the product rule, and simplifying gives:

$$\frac{d^2C}{dX^2} = \Delta^2 e^{-\Delta X}\frac{dC}{dy} + \Delta^2 e^{-2\Delta X}\frac{d^2C}{dy^2} \tag{3.20}$$

Substituting Equation (3.20) into Equation (3.13) and rearranging the equation results in the following transformed form which is the modified Bessel equation:

$$\frac{d^2C}{dy^2} = -\frac{1}{y}\frac{dC}{dy} + \left(\frac{\phi}{\Delta}\right)^2 \frac{1}{y} C \tag{3.21}$$

Equation (3.21) is the equation to be solved, its solution is detailed in section 3.3.

3.3 Model Solution

Equation (3.21) was solved analytically for the concentration profile. The solution is given by Equation (3.22):

$$C = C_1 I_0\left(\frac{2\phi\sqrt{y}}{\Delta}\right) + C_2 K_0\left(\frac{2\phi\sqrt{y}}{\Delta}\right) \tag{3.22}$$

Substituting the expression for y as defined by equation (3.15), the concentration profile is then given by:

$$C = C_1 I_0\left(\frac{2\phi\sqrt{e^{-\Delta}}}{\Delta}\right) + C_2 K_0\left(\frac{2\phi\sqrt{e^{-\Delta}}}{\Delta}\right) \tag{3.23}$$

Where I_0 and K_0 are the zero order modified Bessel functions of the first and second kind respectively. The constants C_1 and C_2 may be determined by applying the following boundary conditions:

$$\text{B.C.1: at } X=0; \qquad \frac{dC}{dX} = -Sh(C_b - C) \tag{3.24}$$

$$\text{B.C.2: at } X=1; \qquad \frac{dC}{dX} = 0 \tag{3.25}$$

Boundary condition 1 (B.C.1) is the Robin type boundary condition in which C_b is the ratio of the bulk concentration to the inlet species concentration and, *Sh* is the Sherwood number defined as:

$$Sh = \frac{k\delta}{D_{AB}} \tag{3.26}$$

Where k is the convective mass transfer coefficient. The Sherwood number takes into account the diffusion resistance in the gas film layer. There are many mass transfer correlations in literature from which the Sherwood number can be calculated. Most studies in gas phase

photocatalytic reactions have used the correlation in Equation 3.27 by Votruba *et al*., (1975). A recent correlation (Equation 3.28) specifically for photocatalytic reactions using TiO_2 coated fibrous catalyst was developed by Malayeri *et al*., (2020).

$$\mathrm{Sh}=0.705\left(\mathrm{Re}\frac{\mathrm{L}}{\delta}\right)^{0.43}\mathrm{Sc}^{0.56} \tag{3.27}$$

$$\mathrm{Sh}=0.0059\mathrm{Re}^{0.4663}\mathrm{Sc}^{\frac{1}{3}} \tag{3.28}$$

where *Re* is the Reynolds number, and *Sc* is the Schmidt number. Applying the boundary conditions results in the following expressions for C_1 and C_2 respectively:

$$C_1=\frac{\mathrm{ShC_bK_1}\left(\frac{2\phi}{\Delta}\sqrt{e^{-\Delta}}\right)}{\mathrm{I_1}\left(\frac{2\phi}{\Delta}\sqrt{e^{-\Delta}}\right)\left[\mathrm{ShK_0}\left(\frac{2\phi}{\Delta}\right)-\phi\mathrm{K_1}\left(\frac{2\phi}{\Delta}\right)\right]+\mathrm{K_1}\left(\frac{2\phi}{\Delta}\sqrt{e^{-\Delta}}\right)\left[\mathrm{ShI_0}\left(\frac{2\phi}{\Delta}\right)+\phi\mathrm{I_1}\left(\frac{2\phi}{\Delta}\right)\right]} \tag{3.29}$$

$$C_2=\frac{\mathrm{ShC_bI_1}\left(\frac{2\phi}{\Delta}\sqrt{e^{-\Delta}}\right)}{\mathrm{I_1}\left(\frac{2\phi}{\Delta}\sqrt{e^{-\Delta}}\right)\left[\mathrm{ShK_0}\left(\frac{2\phi}{\Delta}\right)-\phi\mathrm{K_1}\left(\frac{2\phi}{\Delta}\right)\right]+\mathrm{K_1}\left(\frac{2\phi}{\Delta}\sqrt{e^{-\Delta}}\right)\left[\mathrm{ShI_0}\left(\frac{2\phi}{\Delta}\right)+\phi\mathrm{I_1}\left(\frac{2\phi}{\Delta}\right)\right]} \tag{3.30}$$

Where I_1 and K_1 are the first order modified Bessel functions of the first and second kind respectively.

The effectiveness factor, η may be defined as follows:

$$\eta=\frac{-\mathrm{D_{AB}}\frac{\mathrm{dC_A}}{\mathrm{dx}}}{\mathrm{r_0}}=\frac{-\mathrm{D_{AB}}\frac{\mathrm{dC_A}}{\mathrm{dx}}}{\mathrm{k_rC_bI_v}} \tag{3.31}$$

The reaction rate, r_0 is the ideal rate that would be obtained if the bulk concentration is maintained through the entire photocatalytic film and the incident photon flux does not attenuate through the film.

In dimensionless form equation (3.31) may be written as:

$$\eta = \frac{-1}{\phi^2}\frac{dC}{dX} \tag{3.32}$$

Combining equations (3.23), (3.29), (3.30), and (3.32) results in the following equation for the effectiveness factor:

$$\eta = \frac{1}{\phi}\frac{Sh C_b\left[K_1\left(\frac{2\phi}{\Delta}\sqrt{e^{-\Delta}}\right)I_1\left(\frac{2\phi}{\Delta}\right) - I_1\left(\frac{2\phi}{\Delta}\sqrt{e^{-\Delta}}\right)K_1\left(\frac{2\phi}{\Delta}\right)\right]}{I_1\left(\frac{2\phi}{\Delta}\sqrt{e^{-\Delta}}\right)\left[Sh K_0\left(\frac{2\phi}{\Delta}\right) - \phi K_1\left(\frac{2\phi}{\Delta}\right)\right] + K_1\left(\frac{2\phi}{\Delta}\sqrt{e^{-\Delta}}\right)\left[Sh I_0\left(\frac{2\phi}{\Delta}\right) + \phi I_1\left(\frac{2\phi}{\Delta}\right)\right]} \tag{3.33}$$

An approximation of Equation (3.33) was developed by first linearizing Equation (3.13) using the Taylor series expansion and then solving by the perturbation method.

Firstly, the term $e^{-\Delta x}$ in Equation (3.13) may be linearised using Taylor series expansion:

$$f(x) = f(x_0) + xf'(x_0) + \frac{x^2}{2!}f''(x_0) + \cdots + \frac{x^n}{n!}f^n(x_0) \tag{3.34}$$

$$f(x) = e^{-\Delta x} \tag{3.35}$$

Taylor series truncated to second order gives:

$$e^{-\Delta x} \approx 1 - \Delta x + \frac{\Delta^2 x^2}{2} + \cdots \tag{3.36}$$

Therefore, Equation (3.13) may be written as:

$$\frac{d^2C}{dX^2} = \phi^2 C\left(1 - \Delta x + \frac{\Delta^2 x^2}{2}\right) \tag{3.37}$$

There are several methods by which Equation (3.37) may be solved for the concentration, the simplest method is regular perturbation. The optical thickness is chosen as the perturbation parameter (i.e. Δ is assumed to be very small). Therefore, the proposed perturbation approximation solution is:

$$C = C_0 + \Delta C_1 + \Delta^2 C_2 + \cdots + \Delta^n C_n \tag{3.38}$$

Substituting the truncated Equation (3.38) into Equation (3.37) gives:

$$\frac{d^2}{dX^2}(C_0 + \Delta C_1) = \phi^2 (C_0 + \Delta C_1)\left(1 - \Delta x + \frac{\Delta^2 x^2}{2}\right) \tag{3.39}$$

For Δ^0, Equation (3.39) becomes:

$$\frac{d^2 C_0}{dX^2} - \phi^2 C_0 = 0 \tag{3.40}$$

The general solution of Equation (3.40) may be obtained by D operator method:

$$(D^2 - \phi^2)C_0 = 0 \tag{3.41}$$

Therefore:

$$C_0 = Ae^{\phi x} + Be^{-\phi x} \tag{3.42}$$

And,

$$\frac{dC_0}{dx} = \phi Ae^{\phi x} - \phi Be^{-\phi x} \tag{3.43}$$

The integration constants *A* and *B* may be obtained by applying the boundary conditions B.C.1 and B.C.2, Equations (3.24) and (3.25) respectively.

From Equation (3.43) and subject to the boundary condition in Equation (3.24), the constants A and B are related as:

$$A = \frac{ShC_b - (Sh - \phi)B}{(\phi + Sh)} \tag{3.44}$$

And, using the boundary condition in Equation (3.25), gives:

$$A = Be^{-2\phi} \tag{3.45}$$

Substituting Equation (3.45) into Equation (3.44) and solving for *B* gives:

$$B = \frac{-ShC_b}{e^{-2\phi}(\phi + Sh) + (-Sh - \phi)} \tag{3.46}$$

For Δ^1, Equation (3.39) becomes:

$$\frac{d^2C_1}{dX^2} - \phi^2 C_1 = -\phi^2 C_0 x \tag{3.47}$$

Substituting Equation (3.42) into Equation (3.47) gives:

$$\frac{d^2C_1}{dX^2} - \phi^2 C_1 = -\phi^2 \left(Ae^{\phi x} + Be^{-\phi x}\right)x \tag{3.48}$$

Equation (3.48) is inhomogeneous and thus, its solution will have the complimentary function ($C_{1,CF}$) and the particular integral ($C_{1,PI}$).

Thus:

$$C_1 = C_{1,CF} + C_{1,PI} \tag{3.49}$$

To find $C_{1,CF}$ the right-hand side of Equation (3.48) is assumed to be equal to zero. Therefore the solution for the complimentary function is similar to that of Equation (3.40):

$$C_{1,CF} = De^{\phi x} + Ee^{-\phi x} \tag{3.50}$$

Where *D* and *E* are the integration constants.

To find the particular integral, we make use of the following standard trial function:

$$[F(D)]\{e^{ax}g(x)\} = e^{ax}[F(D) + a]\{g(x)\} \tag{3.51}$$

Thus, from Equations (3.48) and (3.51):

$$(\mathrm{D}^2 - \phi^2)\mathrm{C}_{1,PI} = \text{-}\phi^2\left(Ae^{\phi \mathrm{x}} + Be^{\text{-}\phi \mathrm{x}}\right)x \tag{3.52}$$

Therefore,

$$\mathrm{C}_{1,PI} = \text{-}\phi^2\left\{e^{\phi \mathrm{x}}.A\left[\frac{1}{D^2 + 2\phi D}\right]\{x\} + e^{\text{-}\phi \mathrm{x}}.B\left[\frac{1}{D^2 - 2\phi D}\right]\{x\}\right\} \tag{3.53}$$

$$\frac{1}{D^2 + 2\phi D} = \frac{1}{2\phi D} - \frac{1}{4\phi^2} + \frac{1}{8\phi^3} \tag{3.54}$$

Therefore Equation (3.53) becomes:

$$\mathrm{C}_{1,PI} = \text{-}\phi^2\left\{e^{\phi \mathrm{x}}.A\left[\frac{1}{2\phi D} - \frac{1}{4\phi^2} + \frac{1}{8\phi^3}\right]\{x\} + e^{\text{-}\phi \mathrm{x}}.B\left[-\frac{1}{2\phi D} - \frac{1}{4\phi^2} - \frac{1}{8\phi^3}\right]\{x\}\right\} \tag{3.55}$$

Or,

$$\mathrm{C}_{1,PI} = \text{-}\phi^2\left\{e^{\phi \mathrm{x}}.A\left[\frac{\mathrm{x}^2}{4\phi} - \frac{\mathrm{x}}{4\phi^2} + \frac{1}{8\phi^3}\right] - e^{\text{-}\phi \mathrm{x}}.B\left[\frac{\mathrm{x}^2}{4\phi} + \frac{\mathrm{x}}{4\phi^2} + \frac{1}{8\phi^3}\right]\right\} \tag{3.56}$$

Substituting Equations (3.42), (3.50) and (3.56) into Equation (3.38) gives:

$$C = Ae^{\phi \mathrm{x}} + Be^{\text{-}\phi \mathrm{x}} + \Delta\left[De^{\phi \mathrm{x}} + Ee^{\text{-}\phi \mathrm{x}} - Ae^{\phi \mathrm{x}}\left(\frac{\phi \mathrm{x}^2}{4} - \frac{\mathrm{x}}{4} + \frac{1}{8\phi}\right) + Be^{\text{-}\phi \mathrm{x}}\left(\frac{\phi \mathrm{x}^2}{4} + \frac{\mathrm{x}}{4} + \frac{1}{8\phi}\right)\right] \tag{3.57}$$

And,

$$\frac{dC}{dx} = \phi A e^{\phi x} - \phi B e^{-\phi x} + \Delta \left[\phi D e^{\phi x} - \phi E e^{-\phi x} - A e^{\phi x} \left(\frac{\phi^2 x^2}{4} + \frac{\phi x}{4} - \frac{1}{8} \right) - B e^{-\phi x} \left(\frac{\phi^2 x^2}{4} - \frac{\phi x}{4} - \frac{1}{8} \right) \right] \tag{3.58}$$

At x=0 and substituting Equation (3.45), Equation (3.58) becomes:

$$\frac{dC}{dx} = \phi B \left(e^{-2\phi} - 1 \right) + \phi \Delta \left[(D - E) + \frac{B}{8\phi} \left(e^{-2\phi} + 1 \right) \right] \tag{3.59}$$

Substituting Equation (3.59) into Equation (3.32) gives:

$$\eta = \frac{B}{\phi} \left(1 - e^{-2\phi} \right) - \frac{\Delta}{\phi} \left[(D - E) + \frac{B}{8\phi} \left(e^{-2\phi} + 1 \right) \right] \tag{3.60}$$

Equation (3.60) may be written as:

$$\eta = \frac{B}{\phi} \left[\frac{2\sinh(\phi)}{e^{\phi}} \right] - \frac{\Delta}{\phi} \left[(D - E) + \frac{B}{8\phi} \left(\frac{2\cosh(\phi)}{e^{\phi}} \right) \right] \tag{3.61}$$

The determination of the constants *D* and *E* in Equation (3.61) is tedious. If the ratio $\frac{\Delta}{\phi}$ is very small, the term $-\frac{\Delta}{\phi}(D - E)$ may be ignored. And, with the substitution of Equation (3.46) into Equation (3.61) the asymptotic solution of the effectiveness factor becomes:

$$\eta = \left[\frac{Sh C_b}{\phi [Sh \cosh(\phi) + \phi \sinh(\phi)]} \right] \left[\sinh(\phi) - \frac{\Delta}{8\phi} \cosh(\phi) \right] \tag{3.62}$$

Equation (3.62) may be used for a quick estimation of the effectiveness factor.

Equation (3.33) is the model developed in this work and the main topic in the following sections.

CHAPTER 4
MATERIALS AND METHODS

This project was conducted in two parts; the first was the theoretical development of the model and the second was the experimental validation of the model. This chapter gives details of the experimental part from the design and development of the reactor, the experimental setups and procedures employed for preliminary experiments, and then validation of the model. The details of the theoretical model development including the model basis, assumptions, the overview of the governing equations, and the analytical solution of the model have been given in Chapter 3.

4.1 Reactor Development, Catalyst Preparation and Operation

The gas photocatalytic reactor was not readily available at the commencement of the project. It was, therefore, necessary to design and manufacture a new reactor, including the UV lamps and the catalyst. A combination of reactors found in literature was used to design the ethylene photocatalytic reactor, which was then manufactured by Scientific Manufacturing c.c. (SMC). The reactor casing is cylindrical, 18 cm diameter stainless steel with a length of 33 cm. The UV lamp circuit was constructed using Philips TUV PL-S 5W GERMICIDAL light bulbs (28 mm wide, 67 mm long) with a UV output of 0.18 W and a peak wavelength of 254 nm. These UV light bulbs were sourced from The Lamp House. Other accessories required for a complete lamp circuit and the power supply, such as capacitors, wires, and switches were sourced from Transignal Electrical Sales c.c. The complete setup is depicted in Figure 4.1, where (a) is the power supply unit connected to three UV light bulbs such that one or more lamps can be switched on/off independently; (b) is the reactor casing; (c) is the mass flow controller; (d) is the ethylene analyser; (e) is the temperature sensor, (f) shows the lamps attached to the lid of the reactor casing and (g) shows the lamps/ catalyst arrangement. The reactor was later fitted with a cooling jacket since it was discovered during preliminary experiments that the UV lamps were generating heat inside the reactor. The cooling jacket was also manufactured by SMC.

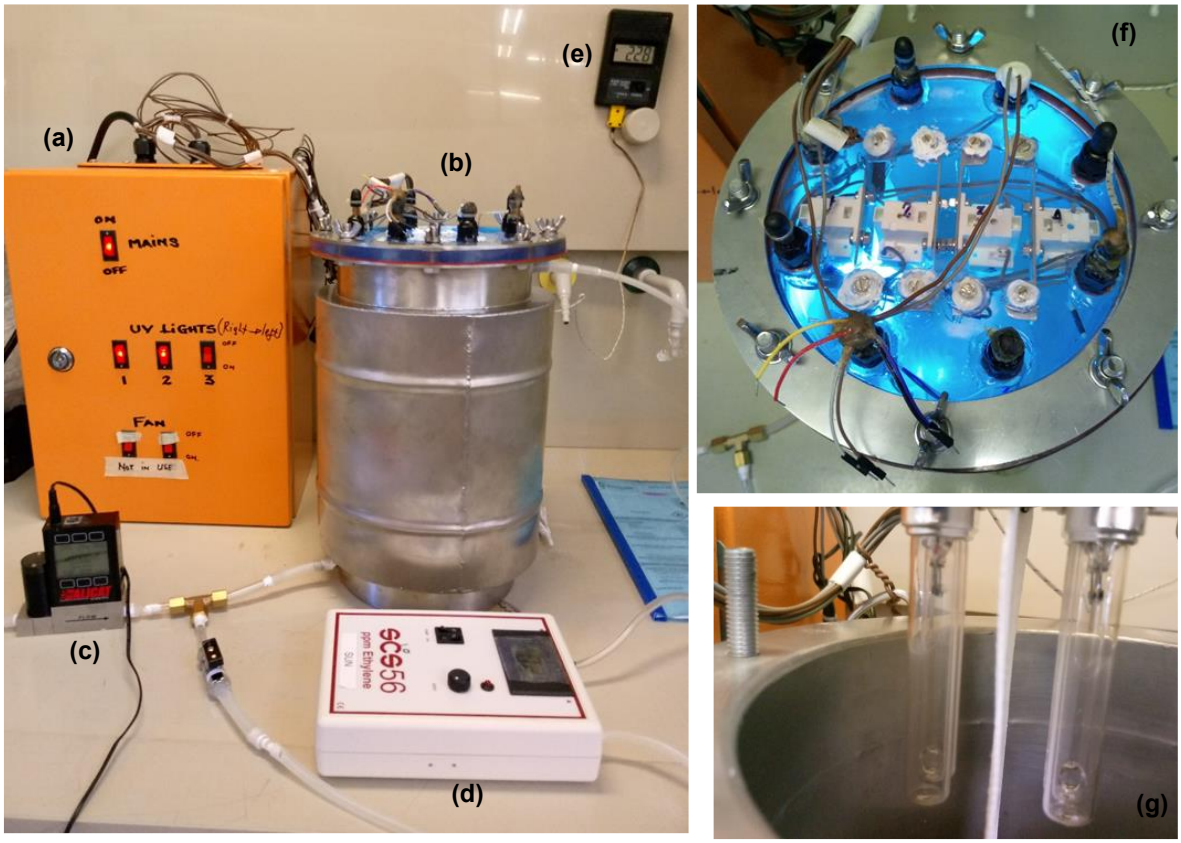

Figure 4. 1: Reactor setup and its components (a) Power supply; (b) Reactor casing; (c) Mass flow controller; (d) Ethylene analyser; (e) Temperature sensor, (f) Lamps attached to the lid of the reactor casing (g) Lamps/ catalyst arrangement.

The catalyst was prepared by depositing the photocatalytic material, Titanium(IV) Oxide, Nanopowder, 21 nm (TiO_2) onto the catalyst support material (batting nonwoven vilene). The method involved dissolving 4.5 g TiO_2 in 100 mL ethanol and then stirring for 30 minutes in a magnetic stirrer. The solution was then coated onto the batting nonwoven vilene (width: 100 mm, length: 135 mm, thickness: ±0.3 mm). The coating was done by soaking the material into the prepared solution overnight, after which the catalyst paste was smoothed over the material to ensure uniform spread. The coated material was then dried with compressed air for a few minutes and then in an oven at 60°C for 2 hours. Before utilized in the experiments the catalyst was exposed to UV light for about 45 minutes to ensure the removal of all the adsorbed ethanol. This catalyst preparation method was adopted from Basso *et al*. (2018) with modifications.

The reactor setup was designed such that it can be operated either in a continuous or batch mode, as indicated in Figure 4.2, where (a) shows the UV lamps/ catalyst arrangement inside the reactor casing, and (b) is the pump used to transport the gas to the ethylene analyser (c).

The pump is a mini diaphragm vacuum pump from Laboport and the ethylene analyser is SCS56 from Gas At Site.

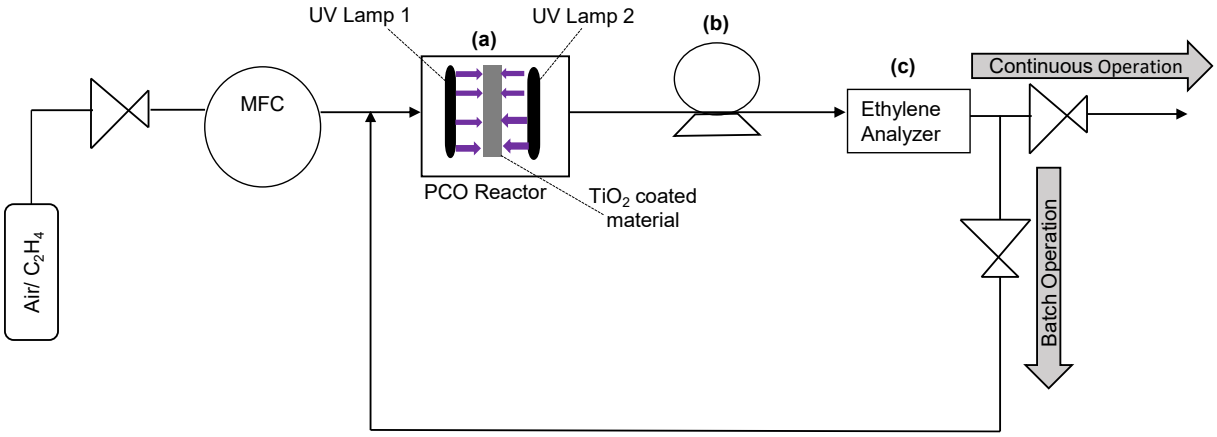

Figure 4. 2: Process operation and experimental setup

The continuous mode of operation was used to test if ethylene can be degraded. The ethylene/ air premixed gas with a concentration of 100 ppm was supplied by Air Liquide. This gas was transported directly from the cylinder situated outside the laboratory through a gas line at a pressure of 100 kPa (gauge) to the reactor and then ethylene analyser. The gas was run through the system continuously with the UV lamps switched off until the analyser read a constant value. This value was then taken as the initial concentration, and only then the UV lamps were switched on. Two UV lamps (lamp 1 and lamp 2) were switched on, with one catalyst sheet in between them. The light intensity between the lamps and the catalyst sheet was measured to be 118.8 W/m^2.

4.2 Experimental setup and procedure for kinetic experiments

As indicated in Figure 4.2, the setup can be operated in batch mode by continuously recycling a fixed volume of gas back to the reactor. A batch operation is necessary to obtain the reaction kinetics for the model validation. Figure 4.3 shows a batch reactor setup used in the experiments to determine the kinetic rate constant. The UV lamps and the catalyst inside the PCO reactor were arranged as shown in Figure 4.1 (g) and Figure 4.2 (a) and all the experiments were run with two lamps and one catalyst in between them. In this setup, a built-in pump within the ethylene analyser was used, which has a fixed flow rate of 0.8 L/min. Small

cylinders of the air/ ethylene gas mix with different ethylene concentrations (10 ppm, 50 ppm, and 100 ppm) were sourced from Air Products.

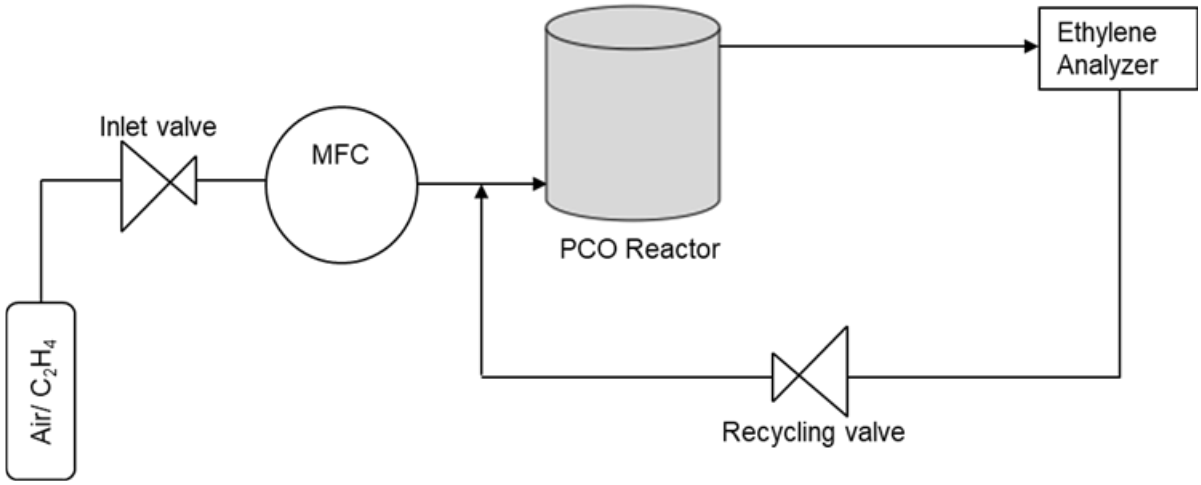

Figure 4. 3: Batch reactor setup

Before running the batch experiments, a calibration test was done to ascertain if the analyser could give a stable initial concentration and repeatability. To do this, the reactor was filled from the 10 ppm cylinder with the MFC set at 0.5 L/min while UV lamps were switched off. During the filling process, both valves were open, and the ethylene analyser pump was running. This was carried on until a constant concentration was achieved, after which the inlet valve was closed. The gas was then recirculated through the reactor and the ethylene analyser for 15 minutes while recording the reading on the analyser every 30 seconds. Following the same operation for the experiments, the reactor was filled with the 50 ppm and 100 ppm cylinders respectively to obtain different initial concentrations. However, the gas was recirculated for about 5 minutes after closing the inlet valve before switching the UV lamps on. The reactor was run with two UV lamps switched on and one catalyst sheet in between them. The catalyst was prepared as described in section 4.2. The experiments were run using three different initial concentrations (34.5 ppm, 49.9 ppm, and 60.4 ppm). The initial concentration of 34.5 ppm was obtained from the 50 ppm cylinder and the 100 ppm cylinder was used to obtain the initial concentration of 49.9 ppm and 60.4 ppm respectively. In all the experiments the changes in concentration were recorded every 30 seconds until a constant reading of ethylene was obtained. The experiments with the initial concentration of 34.5 ppm were repeated four times (Runs 1 – 4) using the same catalyst, however, before being utilized in Run 4 the catalyst was regenerated by exposing it to UV light for 30 minutes with no gas in the reactor. Run 5 (C_{A0} =

49.9 ppm) and Run 6 (C_{A0} = 60.4 ppm) were done once using a newly prepared catalyst which was regenerated in between the two runs.

4.3 Experimental Limitations

The method for the preparation of the catalyst was chosen for its simplicity and it used only one reagent, hence limited impurities to get rid of. The catalyst was carefully prepared to ensure uniform coating by using the same amount of solution for each coating, and soaking was done in containers of the same size and shape. However, there may be inconsistencies during the smoothing process as this was done manually with a brush. To reduce the impact of this on the results, the same catalyst sheet was used for the first four runs (1 – 4) and another for the last two runs (5 and 6). It was also important to keep the reactor closed to avoid interference of outside air with the reaction. The reactor was opened to change the catalyst for the last two runs, and some air was introduced into the reactor; hence, there was a difference in the results compared to the first four runs. Although the initial concentrations were different in runs 5 and 6, the expected results of the rate constant were achieved. The flow rate could not be varied as it was dependent on the analyser flow rate which is fixed.

CHAPTER 5
RESULTS AND DISCUSSION

This chapter discusses the theoretical evaluation and comparison of the new model with other available models, and the results of the experimental validation. It begins by comparing the effectiveness factor given by the new model with that of the asymptotic solution, also derived in this work. The new model is then validated and compared with the literature. It is then used in the analysis of the different parameters affecting the operation of photocatalytic reactors. These parameters include the Thiele modulus, the optical thickness, and the Sherwood number. The experimental validation section involves the determination of the reaction kinetic constant and the comparison of the reaction rate calculated by the model and that obtained experimentally. Finally, Damköhler's number is briefly discussed to show the application of the model in reactor design and scale up.

5.1 Validation and analysis of the new model against other models

Equation (3.62) was derived using the Taylor series and the perturbation method. It is applicable only for small optical thickness values in the range of $0.00625 > \Delta < 0.2$. Table 5.1 shows how the results of Equation (3.62) compare with those of Equation (3.33). The two solutions are comparable with a very small root mean square error (RMSE = 0.2571).

Table 5. 1: Comparison of analytical and asymptotic solutions (Sh = 0.001, Δ = 0.1)

	Effectiveness Factor	
Thiele Modulus	**Analytical solution**	**Asymptotic solution**
0.001	0.95072	0.98649
0.005	0.92951	0.97509
0.01	0.86891	0.90893
0.05	0.28156	0.28563
0.1	0.09046	0.09087
0.5	0.00398	0.00397
1	0.00099	0.00098
1.5	0.00044	0.00040
2	0.00025	0.00016

The calculations of the current model (Equation 3.33) give exact values when compared to the analytical solution of Visan et al. (2014) as well as the numerical solution of Edwards et al. (1996). This is illustrated in Table 5.2 for different values of the optical thickness. Thiele modulus of 0.05 is used in the calculations for comparison since the data from Edwards et al., (1996) are reported at this value. The exact values are obtained starting from a cut-off Sherwood value of 0.55, beyond which the present model converges with the other models.

Table 5. 2: Comparison of the current model with other models (ø = 0.05)

	Effectiveness Factor				
			Current Model		
Optical Thickness	Visan (2014)	Edwards (1996)	Sh = 0.55	Sh = 0.01	Sh = 0.001
0.1	0.94989	-	0.94680	0.76826	0.28156
1	0.63086	0.6319	0.63007	0.54566	0.24494
3	0.31570	0.3167	0.31625	0.29346	0.17675
5	0.19765	-	0.19846	0.18924	0.13272
7	0.14173	0.1427	0.14263	0.13781	0.10519
10	0.09899	0.1	0.09995	0.09756	0.07999

As can be seen in Table 5.2, the current model deviates from (Visan *et al*., 2014) and (Edwards *et al*., 1996) for low values of the Sherwood number where external mass transfer limitations are expected because these models only account for internal diffusion resistances. Hence, the low values of the Sherwood number are the novelty of the model in this work. The calculations of the model presented by Rawlings & Ekerdt (2002: 386) which is also based on the Robin boundary condition for first order reaction in a spherical catalyst, compare well with the current model at low Sherwood numbers in Table 5.3. This model in Rawlings & Ekerdt (2002: 386) is for conventional reactors not utilizing photons, hence its applicability to the current model is limited to operations at low optical thickness. The closely comparable values of the effectiveness factor in Table 5.3 provide confidence in the model presented in this article.

Table 5. 3: Comparison of the current model for low Sh ($\phi = 0.05, \Delta = 0.1$)

Sh	Rawlings & Ekerdt (2002)	Current Model
0.55	0.99399	0.94680
0.01	0.79904	0.76826
0.001	0.28560	0.28156

5.2 Effect of design parameters on the effectiveness factor

The developed model in Equation (3.33) can predict the three operating regions similar to the conventional reactors not utilizing photons as shown in Figure 5.1. In region 1 ($\phi < 0.1$) there is minimal internal diffusion resistance, and the process is reaction rate controlled at the catalyst surface. In region 2 ($0.1 < \phi < 1$) the process is limited by the reaction rate and region 3 ($\phi > 1$) is where internal diffusion resistance is very high.

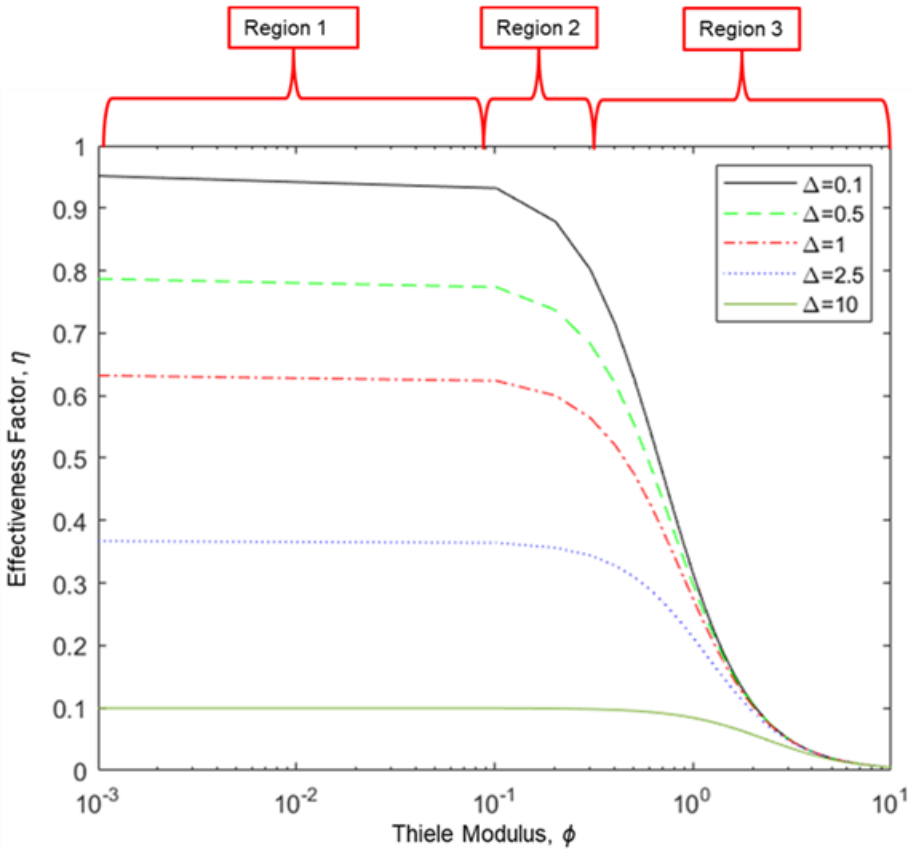

Figure 5. 1: Effectiveness factor vs Thiele Modulus at different values of the optical thickness (Sh = 0.55)

It is also shown in Figure 5.1 that the effectiveness factor decreases with an increase in optical thickness. The optical thickness is one of the most important and complex design parameters of photocatalytic reactors. It is the distance that the photons must travel to be absorbed by the catalyst coating. In Figure 5.2 the sensitivity of the effectiveness factor on the optical thickness seems to level off at low Sherwood numbers meaning that the low effectiveness factors are attributed to the external mass transfer limitations.

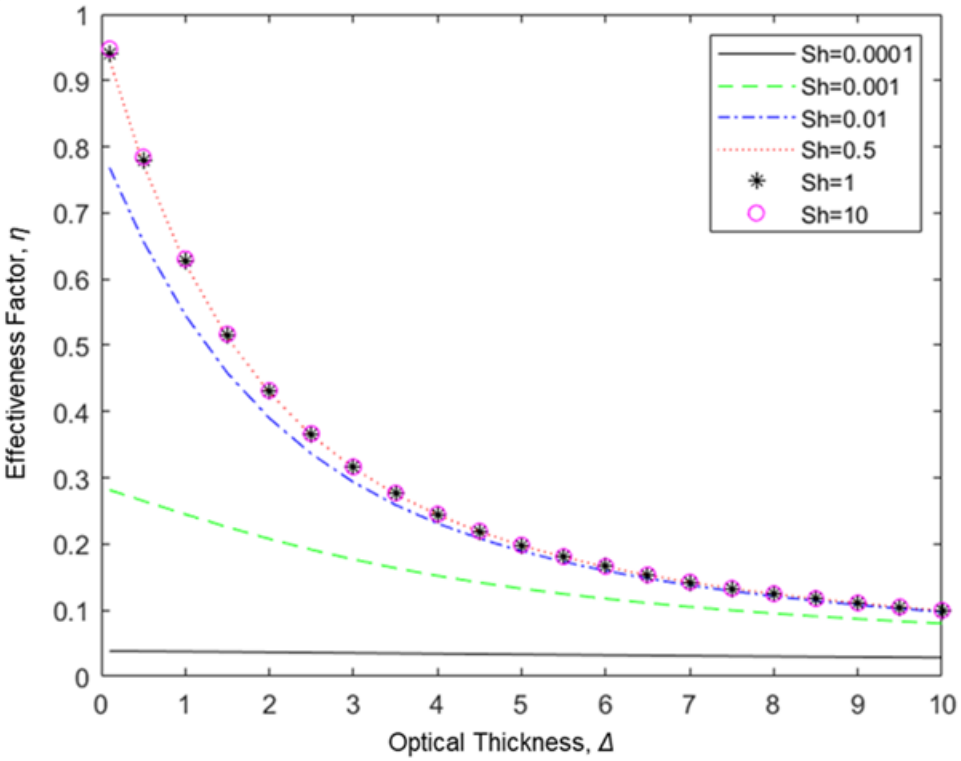

Figure 5. 2: Effect of Sherwood number on effectiveness factor for ϕ = 0.1

These effects of the external mass transfer resistance can be seen in Figure 5.3 by evaluating the effect of the Sherwood number on the three regions described in Figure 5.1. The Sherwood number lumps together the effect of the external mass transfer resistances in the ratio of the convection rate to the diffusion rate. Region 1 as described in Figure 5.1 exists in Figure 5.3 only at high values of Sherwood number starting from the cut-off value. At low Sherwood numbers, this region shifts towards lower ranges of Thiele Modulus, and the free internal diffusion region becomes smaller. The rate of diffusion is high when the Sherwood number is low, but the rate of convection is low. Thus, in this region, the limitation is low transport of the bulk substrate which adversely affects the internal diffusion due to insufficient substrate availability. With regards to regions 2 and 3, the effectiveness factor decreases rapidly with an increase in the Thiele Modulus as the Sherwood number is decreased. There is little distinction between these two regions also due to the limited transport of the bulk substrate. In general, the external mass transfer limitations become significant at low Sherwood numbers, due to convective mass transport limitations. Looking at the graphs of Sh = 0.1 and Sh = 0.01 in Figure 5.3, the rapid decrease of the effectiveness factor starts at ϕ = 0.1 as the Sherwood number is decreased. This is the transition point from which the different controlling mechanisms can be described. Table 5.4 gives a summary of the possible mechanisms controlling the reaction rate of the photocatalyst layer.

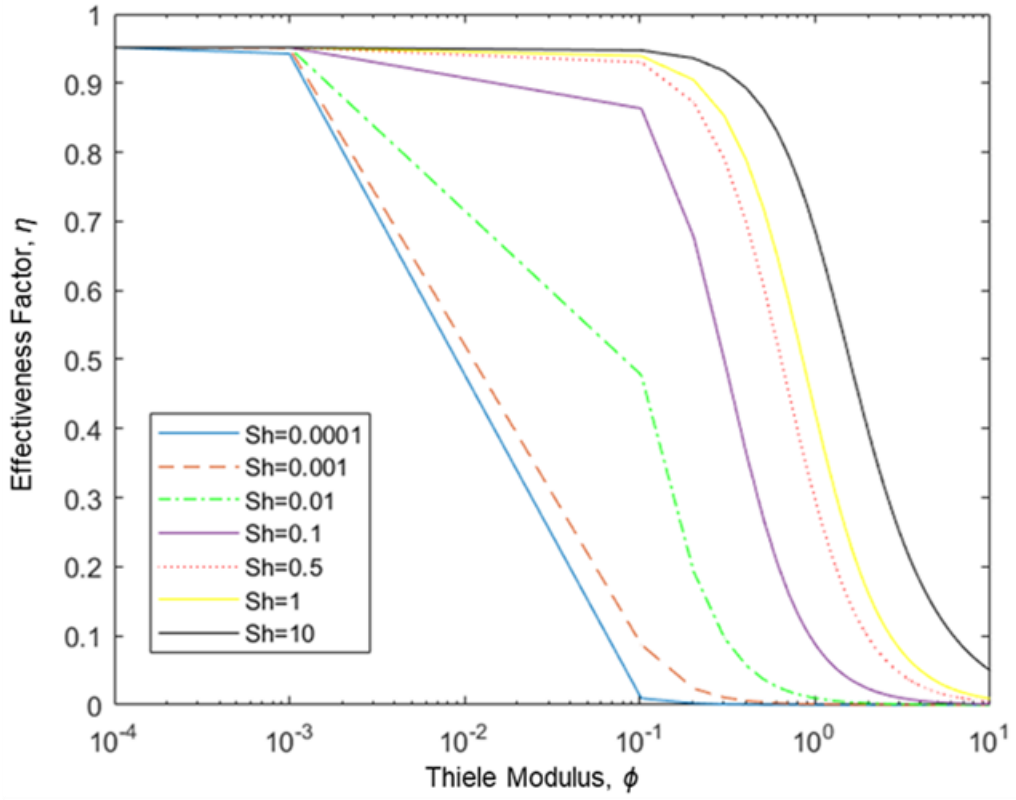

Figure 5. 3: The effect of the Sherwood number on the effectiveness factor for Δ = 0.1

Table 5. 4: Controlling mechanisms for photocatalyst layer reaction rate

Sherwood Number	Thiele Modulus	Controlling Mechanism
$\mathrm{Sh} < 0.1$	$\phi < \mathrm{Sh}$	Reaction
	$\mathrm{Sh} < \phi < 0.1$	External mass transfer
	$0.1 < \phi$	External mass transfer and internal diffusion
$0.1 < \mathrm{Sh}$	$\phi < 0.1$	Reaction
	$0.1 < \phi < \mathrm{Sh}$	Internal diffusion
	$\mathrm{Sh} < \phi$	Internal diffusion and external mass transfer

It is also possible that the optical thickness plays a role in the decreased effectiveness factor as it is expected that the photocatalyst surface area becomes less illuminated as the optical thickness is increased. This may lead to fewer photons being absorbed such that only a small area of the catalyst may be activated to initiate the photocatalytic reaction. Thus, further investigations are required to determine the significance of the influence of the two parameters, the Sherwood number, and the optical thickness.

5.3 Experimental validation of the model

The model was validated by comparing the reaction rate obtained experimentally (r_{actual}) with that predicted by the model ($r_{predicted}$). The predicted reaction rate was determined by taking the product of the model effectiveness factor and the reaction rate using the equation:

$$r_{predicted} = \eta(k_r C_{A0}) \tag{5.1}$$

The reaction rate constant (k_r) in Equation (5.1) was determined experimentally using the integral method based on the assumption of a first order reaction. Figure 5.4 shows linear plots obtained for four different runs with the same initial concentration (±34.0 ppm), all with the R^2 value close to 1, implying that the reaction is first order. Figure 5.5 shows similar plots for the initial concentrations of 49.9 ppm and 60.4 ppm respectively and they also show high R^2 values.

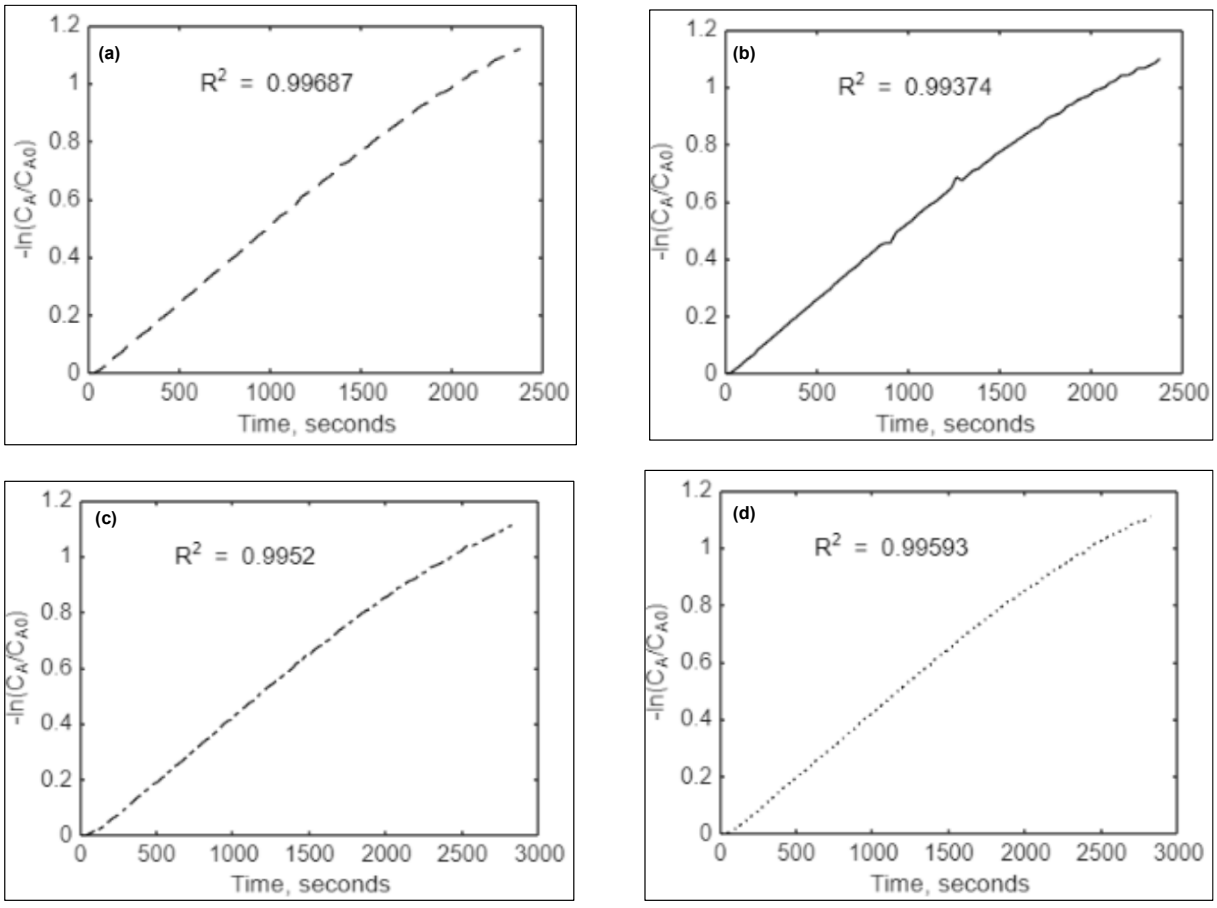

Figure 5. 4: First order plots for Runs 1 - 4 (a) Run 4 (C_{A0} = 34.0 ppm); (b) Run 1 (C_{A0} = 34.5 ppm); (c) Run 2 (C_{A0} = 34.6 ppm); (d) Run 3 (C_{A0} = 34.5 ppm)

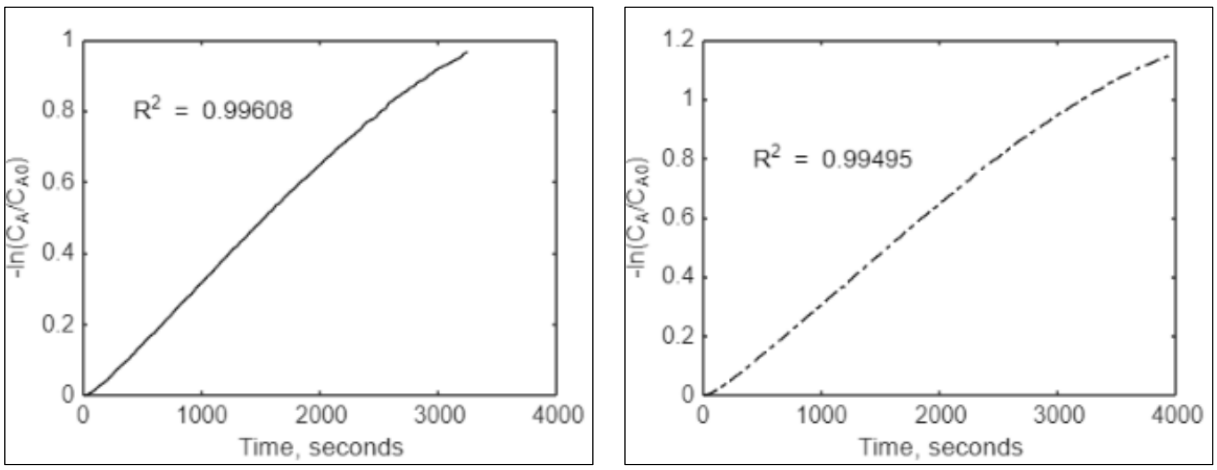

Figure 5. 5: First order plots (a) Run 5 (C_{A0} = 49.9 ppm); (b) Run 6 (C_{A0} = 60.4 ppm)

The experimentally obtained k_r value was then used to calculate the Thiele modulus (Equation 3.14) needed to determine the effectiveness factor (Equation 3.33). The parameter values used in the calculation of the Thiele modulus and the effectiveness factor are given in Table 5.5.

Table 5. 5: Parameter values used to determine the effectiveness factor

Parameter	Symbol	Unit	Value
Diffusion coefficient	D_{AB}	m^2/s	1.56×10^{-5}
Kinematic viscosity	v	m^2/s	8.77×10^{-6}
Catalyst thickness	δ	m	1×10^{-6}
Catalyst length	L	m	0.135
UV light intensity	I_v	W/m^2	118.8
Light absorption coefficient	μ	m^{-1}	6.26×10^{5}
Average pore radius	$\bar{r}$	m	1×10^{-6}
Reactor height	h	m	0.33
Reactor diameter	d	m	0.18
Gas flow rate	Q	m^3/s	1.33×10^{-5}
Reynolds number	Re	Dimensionless	5.96
Schmidt number	Sc	Dimensionless	0.56
Peclet number	Pe	Dimensionless	3.35

Table 5.6 summarizes the rate constant values obtained from the different runs, the actual reaction rate, and the theoretical reaction rate as predicted by the model. The reaction rate predicted by the model is comparable with that obtained experimentally. The theoretical evaluation of the model in Section 5.1 revealed that the new model was not comparable with literature at low Sherwood numbers coinciding with the existence of the external mass transfer limitations, the novelty of this work. The fact that experimental and predicted reaction rates are comparable with Sh of approximately 0.01 indicated in Table 5.6 shows that the model is valid and accounts for the external mass transfer limitations. Also, based on the controlling mechanisms in Table 5.4 and the values of ϕ and Sh in Table 5.6, indicate that the predominant controlling mechanism is the external mass transfer.

Table 5. 6: Reaction Kinetics (Sh = 0.0112, Δ = 0.6264)

Run	C_{A0} (ppm)	K_r (s^{-1})	ϕ	η	$r_{predicted}$ (ppm/s)	r_{actual} (ppm/s)
1.	34.5	0.0005	0.09	0.4931	0.008506	0.0130
2.	34.6	0.0004	0.08	0.5287	0.007317	0.0104
3.	34.5	0.0004	0.08	0.5287	0.007295	0.0104
4.	34.0	0.0005	0.09	0.4931	0.008382	0.0124
5.	49.9	0.0003	0.07	0.5698	0.008529	0.0118
6.	60.4	0.0003	0.07	0.5698	0.010324	0.0135

Theoretically, the reaction rate constant remains constant regardless of the amount of initial concentration. However, a variation in the rate constants is seen in Table 5.6 with a $9x10^{-8}$ variance between the different runs. This result can be attributed to the catalyst preparation and its activity. In Figure 5.5 all four runs were done using the same catalyst with approximately the same initial concentration for each run. During Run 1, the catalyst was used for the first time and was highly active, while its activity had reduced before being utilized in Run 2 and Run 3. Before use in Run 4, the same catalyst was reactivated by exposure to UV light and it can be seen in Figure 5.6 that the performance of the catalyst was similar to that of a new catalyst (Run 1). This result is in agreement with Jeong *et al*. (2013) that the catalyst may be reactivated by exposing the catalyst to UV light or heating at high temperatures. Thus, the catalyst deactivation is one of the reasons for the lower reaction rate constant, and therefore, the reaction rate, in Runs 2 and 3.

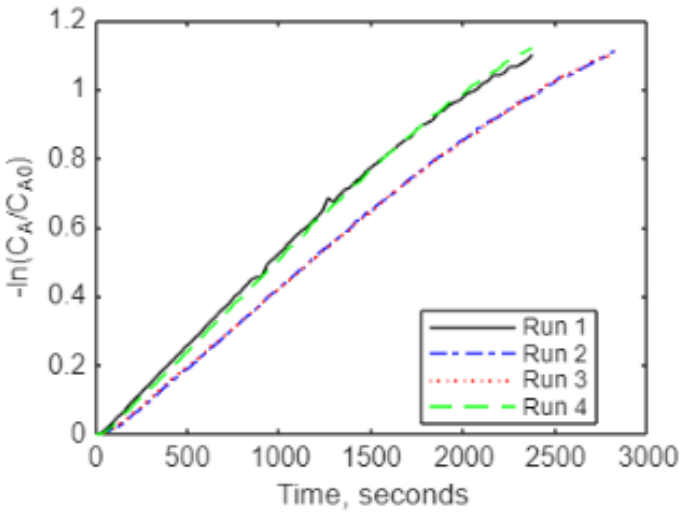

Figure 5. 6: Kinetics plots for 1st order reaction at same initial concentrations (C_{A0} = ±34.0 ppm)

Figure 5.7 shows the results for three different initial concentrations. The difference in the results can be attributed to the quality of the catalyst.

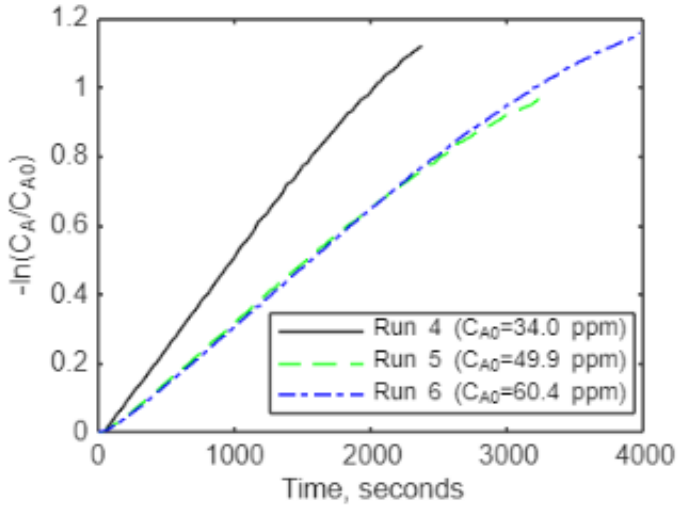

Figure 5. 7: Kinetics plots for 1st order reaction at different initial concentrations

Although the same method was followed when preparing the two photocatalysts (one used in Run 4 and one used in Runs 5 and 6), consistency in achieving the same surface morphology may not be guaranteed. This is because the properties of the deposited photocatalyst layer may change significantly if the preparative conditions vary only slightly, even if the same deposition method is used (Camera-Roda & Santarelli, 2007). The SEM images in Figure 5.8

are for two photocatalyst sheets, both prepared by the same methodology described in Chapter 4. However, the two samples in Figure 5.8 show different surface morphologies both with nonhomogeneous deposition. The formation of TiO_2 aggregates is also evident, thus a decrease in the absorption of light by the photocatalyst due to scattering is possible (Basso *et al*., 2018). The TiO_2 catalyst used is a mixture of anatase and rutile and the different morphologies result from these phases naturally forming individual agglomerates, due to the small particle size (21 nm). The variations in the photocatalyst morphology, crystal phase, specific surface area, and particle aggregate size qualitatively contribute to the differences in photocatalytic activities (Mills & Le Hunte, 1997).

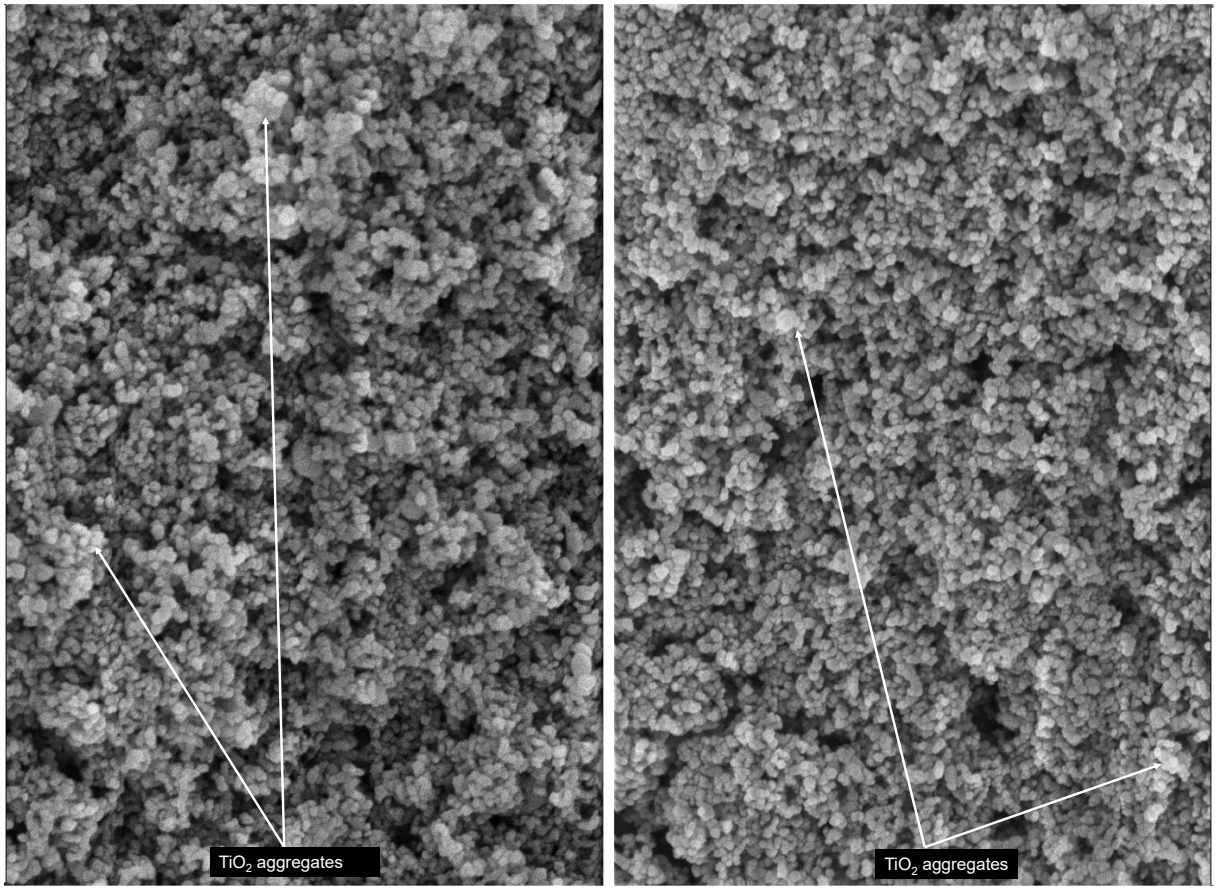

Figure 5. 8: Surface morphology of two TiO_2 photocatalyst samples

It is also observed in Figure 5.7 that the activity of the catalyst used in Runs 5 and 6 could be maintained by exposing it to UV light between runs as the catalyst performance did not deteriorate and the rate constant remained constant as expected. The same catalyst was used in these two runs and thus, the surface morphology did not have an effect. There is also the

possibility of the optical thickness affecting the catalyst area that may be activated discussed in section 5.2. However, the effect of the optical thickness was not experimentally evaluated in this work.

5.4 Application of the model in reactor design and scale up

The developed model may be applied in the design and scaling up of photocatalytic reactors using Damköhler's number (*Da*). To account for the limitations of the catalyst and the photon absorption the developed effectiveness factor must be incorporated into the design equations. Equations (5.2) and (5.3) are the modified design equations for first order CSTR and PFR respectively and were used to develop the plots in Figures 5.9, 5.10, and 5.11.

$$Da = \frac{X_A}{(1 - X_A)\eta} = k_r\tau \tag{5.2}$$

$$Da = \frac{1}{\eta} ln \frac{1}{1 - X_A} = k_r\tau \tag{5.3}$$

Where X_A is the conversion of the pollutant, τ is the space time defined as the ratio of the reactor volume to the volumetric flowrate.

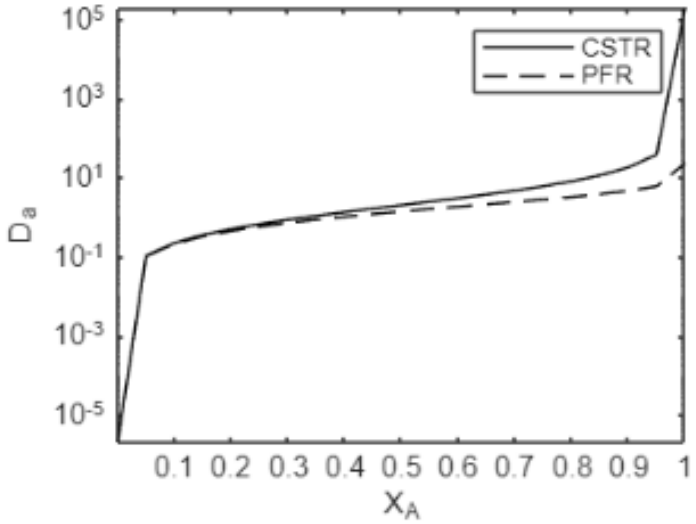

Figure 5. 9: Da vs X (η = 0.4931)

Figure 5.9 is useful in reactor scaling up operations. With the knowledge of the kinetics the optimum reactor size and the volumetric flow rate can be obtained using Damköhler's number. For the laboratory scale reactor used in this work to obtain ethylene reaction kinetics, the *Da* value is 0.315, indicating a very low ethylene conversion based on Figure 5.9. Increasing the reactor volume would increase *Da* and therefore ethylene conversion. Figures 5.10 and 5.11 show the importance of incorporating the effectiveness factor into the reactor design equations. According to Equations (5.2) and (5.3), Damköhler's number is inversely proportional to the effectiveness factor. This is not explicit in Figures 5.10 and 5.11, because the effectiveness factor values determined using the kr values in Table 5.5 do not differ much. Thus, although the reaction rate constant varied for the different runs discussed above, the magnitude of the variation is not significant. The knowledge of the relationship between *Da* and the effectiveness factor is useful for estimating the correct reactor sizing and reactor type suitable for a particular system.

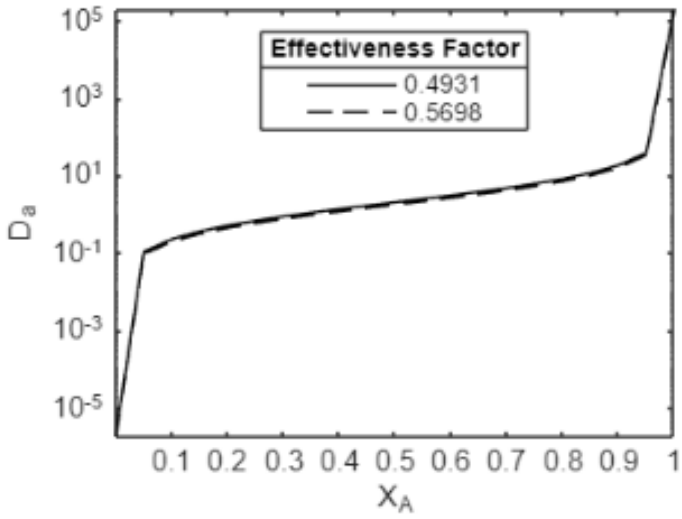

Figure 5. 10: Da vs X_A at different effectiveness factors for CSTR

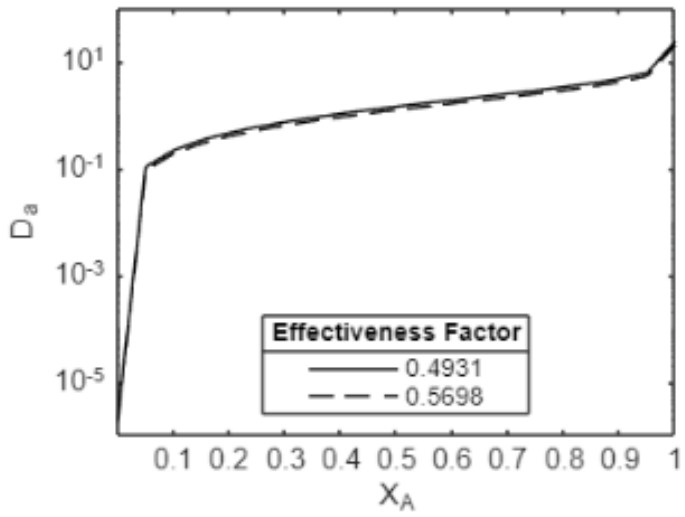

Figure 5. 11: Da vs X_A at different effectiveness factors for PFR

In conclusion, the asymptotic solution was shown to compare well with the exact analytical solution at extremely low optical thickness. This is an important result for a practicing engineer who would require a quick estimation with the same accuracy. Future research can evaluate the actual ranges of the optical thickness at which this approximation would be valid. The new model has been shown to compare well with other models to some extent and was able to predict the experimental reaction rates, thus a model for ethylene photocatalytic oxidation has been found that can account for external mass transfer limitations.

CHAPTER 6
CONCLUSIONS AND RECOMMENDATIONS

6.1 Conclusions

An analytical solution for the differential mass balance equation that accounts for the limitations of the external mass transfer is developed in this study for reactions following the first order kinetics. Theoretical evaluation of the model shows that it compares well with the models found in the literature, where the external mass transfer limitations are not accounted for. This is true at the Sherwood number cut-off point of 0.55 and beyond. It has been shown that the external mass transfer limitations cannot be neglected at low values of the Sherwood number. Therefore, the Sherwood number is one of the important design parameters to be included in the models for evaluating the effectiveness factor. In this work, the Sherwood number of 0.0112 was obtained from the experimental parameters. This is the value that was used in the estimation of the reaction rate by the developed model, thus the model could predict the reaction rate that is comparable to the actual rate at the Sherwood number lower than the cut-off point, the region where external mass transfer limitations prevail. Thus, a mathematical model has been found in this study that accounts for the external mass transfer limitations for ethylene photocatalytic oxidation. The expressions for both diffusional and external resistances are combined in one equation, thus the model can accommodate cases where either only diffusional or external or both resistances are present. The experimental results showed that the controlling mechanism for the photocatalytic layer reaction rate for the tested parameters (Sh = 0.0112 and ϕ in the ranges 0.07 – 0.09) is in the region ($Sh<\phi<0.1$), implying an external mass transfer mechanism.

6.2 Recommendations

The incorporation of the model in the calculation of Da resulted in reasonable design graphs relating the Damköhler's number and ethylene conversion for both CSTR and PFR. This opens opportunities for further work, where the model developed in this work could be used to find the optimum reactor volume that would result in favourable ethylene conversion while considering the possible external mass transfer limitations. Such a reactor must then be built and tested experimentally to determine if the theoretical predictions could be achieved. However, an issue with photocatalytic reactors, in general, is the penetration depth of the UV light through the catalyst, and other future work could explore multiple microreactors operated in parallel to achieve the desired throughput rates.

From the kinetic experiments, it was observed that the catalyst could be reactivated by exposing it to UV light while there was no gas inside the reactor. It is therefore recommended that the activity of the catalyst be maintained by reactivating the catalyst every 2 hours. This time is based on the average duration of the experimental runs done in this work and further work is recommended to ascertain the time intervals between reactor operation and reactivation. It is also necessary to determine the number of times a specific catalyst could be reactivated before it is rendered unusable. The catalyst reactivation can be achieved by switching the gas flow off while the UV light is kept on for at least 30 minutes. The catalyst preparation method should be automated to ensure consistent production of the same quality. Binding material is necessary to ensure that the TiO_2 does not fall off the support material. For the kinetic experiments to be run in a complete batch reactor without recycling, an ethylene sensor that can be installed inside the reactor is required. The proposed sensor was developed in this work although more calibration tests are still required. The details of the sensor development are in the Appendix.

The theoretical evaluation of the model revealed the possibility of the optical thickness affecting the amount of catalyst illuminated area, further research should include investigating this parameter together with the Sherwood number. This may involve optimizing the intensity of the light source and the thickness of the catalyst coating to enhance the light absorption which will improve the efficiency of the catalyst. Another important result, especially for industry applications where quick decisions are usually required is the approximation solution obtained by the perturbation method. This solution is accurate at extremely low optical thickness and future research can evaluate the actual ranges of the optical thickness at which this approximation would be valid and compare these with the theoretical values obtained in this work.

REFERENCES

Bailén, G., Guillén, F., Castillo, S., Serrano, M., Valero, D. & Martínez-Romero, D. 2006. Use of Activated Carbon inside Modified Atmosphere Packages To Maintain Tomato Fruit Quality during Cold Storage. *Journal of Agricultural and Food Chemistry*, 54(6): 2229–2235.

Basso, A., de Fátima Peralta Muniz Moreira, R. & José, H.J. 2018. Effect of operational conditions on photocatalytic ethylene degradation applied to control tomato ripening. *Journal of Photochemistry and Photobiology A: Chemistry*, 367(August): 294–301. https://doi.org/10.1016/j.jphotochem.2018.08.027

Batault, F., Héquet, V., Raillard, C., Thévenet, F., Locoge, N. & Le Coq, L. 2017. How chemical and physical mechanisms enable the influence of the operating conditions in a photocatalytic indoor air treatment device to be modeled. *Chemical Engineering Journal*, 307: 766 – 775.

Biard, P.F., Bouzaza, A. & Wolbert, D. 2007. Photocatalytic degradation of two volatile fatty acids in an annular plug-flow reactor; kinetic modeling and contribution of mass transfer rate. *Environmental Science and Technology*, 41(8): 2908–2914.

Blidi, A. El, Rigal, L., Malmary, G., Molinier, J. & Torres, L. 1993. Ethylene removal for long term conservation of fruits and vegetables. *Food Quality and Preference*, 4: 119 – 126.

Camera-Roda, G. & Santarelli, F. 2007. Optimization of the thickness of a photocatalytic film on the basis of the effectiveness factor. *Catalysis Today*, 129: 161–168.

Chen, C., Wang, Z., Ruan, S., Zou, B., Zhao, M. & Wu, F. 2008. Photocatalytic degradation of C.I. Acid Orange 52 in the presence of Zn-doped TiO_2 prepared by a stearic acid gel method. *Dyes and Pigments*, 77(1): 204–209.

Chen, D., Li, F. & Ray, A.K. 2000. Effect of mass transfer and catalyst layer thickness on photocatalytic reaction. *AIChE Journal*, 46(5): 1034–1045.

De Chiara, M.L.V., Pal, S., Licciulli, A., Amodio, M.L. & Colelli, G. 2015. Photocatalytic degradation of ethylene on mesoporous TiO_2/SiO_2 nanocomposites: Effects on the ripening of mature green tomatoes. *Biosystems Engineering*, 132: 61–70. http://dx.doi.org/10.1016/j.biosystemseng.2015.02.008

De Chiara, M.L.V., Spremulli, L., Licciulli, A., Amodio, M.L. & Colelli, G. 2018. Design and optimization of fluidized bed photoreactor for ethylene reduction within cold storage room for fruits and vegetables using TiO_2-based materials. *Acta Horticulturae*, 1194: 623–629.

Dijkstra, M.F.J., Panneman, H.J., Winkelman, J.G.M., Beenackers, A.A.C.M. & Kelly, J.J. 2002. Modeling the photocatalytic degradation of formic acid in a reactor with immobilized catalyst. *Chemical Engineering Science*, 57(22–23): 4895–4907.

Edwards, M.E., Villa, C.M., Hill, C.G. & Chapman, T.W. 1996. Effectiveness factors for photocatalytic reactions occurring in planar membranes. *Industrial and Engineering Chemistry Research*, 35(3): 712–720.

Einaga, H., Tokura, J., Teraoka, Y. & Ito, K. 2015. Kinetic analysis of TiO2-catalyzed heterogeneous photocatalytic oxidation of ethylene using computational fluid dynamics. *Chemical Engineering Journal*, 263: 325–335. http://dx.doi.org/10.1016/j.cej.2014.11.017

Etacheri, V., Di Valentin, C., Schneider, J., Bahnemann, D. & Pillai, S.C. 2015. Visible-light activation of TiO_2 photocatalysts: Advances in theory and experiments. *Journal of Photochemistry and Photobiology C: Photochemistry Reviews*, 25: 1–29.
Farrauto, R.J., Dorazio, L. & Bartholomew, C.H. 2016. *Introduction to Catalysis and Industrial Catalytic Processes*. Hoboken, New Jersey: John Wiley & Sons, Inc.

Fogler, H.S. 2020. *Elements of Chemical Reaction Engineering*. 6th ed. Pearson Education, Inc.

Fonseca, J. de M., Alves, M.J. dos S., Soares, L.S., Moreira, R. de F.P.M., Valencia, G.A. & Monteiro, A.R. 2021. A review on TiO2-based photocatalytic systems applied in fruit postharvest: Set-ups and perspectives. *Food Research International*, 144(February).

Fu, Y., Shao, L., Liu, Hui, Tong, L. & Liu, Hong. 2011. Ethylene removal evaluation and bacterial community analysis of vermicompost as biofilter material. *Journal of Hazardous Materials*, 192(2): 658–666. http://dx.doi.org/10.1016/j.jhazmat.2011.05.064

Hill, C.G. & Root, T.W. 2014. *Introduction to chemical engineering kinetics and reactor design*. 2nd Edition. Hoboken, New Jersey: John Wiley & Sons.

Hua, L., Li, N., Zhang, W., Ruan, C.Q. & Zeng, K. 2024. Photocatalytic ethylene scavenging for fresh produce preservation: A comprehensive review. *Trends in Food Science and Technology*, 150.

Hussain, M., Akhter, P., Iqbal, J., Ali, Z., Yang, W., Shehzad, N., Majeed, K., Sheikh, R., Amjad, U.E.S. & Russo, N. 2017. VOCs photocatalytic abatement using nanostructured titania-silica catalysts. *Journal of Environmental Chemical Engineering*, 5(4): 3100–3107.

Hussain, M., Ceccarelli, R., Marchisio, D.L., Fino, D., Russo, N. & Geobaldo, F. 2010. Synthesis, characterization, and photocatalytic application of novel TiO2 nanoparticles. *Chemical Engineering Journal*, 157(1): 45–51.

Keller, N., Ducamp, M.N., Robert, D. & Keller, V. 2013. Ethylene removal and fresh product storage: A challenge at the frontiers of chemistry. Toward an approach by photocatalytic oxidation. *Chemical Reviews*, 113(7): 5029–5070.

Kim, S., Jeong, G.H. & Kim, S.W. 2019. Ethylene Gas Decomposition Using ZSM-5/WO3-Pt-Nanorod Composites for Fruit Freshness. *ACS Sustainable Chemistry and Engineering*, 7(13): 11250–11257.

Krivec, M., Pohar, A. & Dra, G. 2015. Hydrodynamics, Mass Transfer, and Photocatalytic Phenol Selective Oxidation Reaction Kinetics in a Fixed TiO_2 Microreactor. *AIChE Journal*, 61(2): 572 – 581.

Levenspiel, O. 1980. The coming-of-age of chemical reaction engineering. *Chemical Engineering Science*, 35(9): 1821–1839.
https://linkinghub.elsevier.com/retrieve/pii/0009250980801321

Li Puma, G. 2005. Dimensionless analysis of photocatalytic reactors using suspended solid photocatalysts. *Chemical Engineering Research and Design*, 83(A7): 820–826.

Licciulli, A., Riccardis, A. De, Pal, S., Nisi, R., Mele, G. & Cannoletta, D. 2017. Ethylene photo-oxidation on copper phthalocyanine sensitized TiO_2 films under solar radiation. *Journal of Photochemistry and Photobiology A: Chemistry*, 346: 523–529.
http://dx.doi.org/10.1016/j.jphotochem.2017.06.046

Lin, Y.T., Weng, C.H. & Chen, F.Y. 2014. Key operating parameters affecting photocatalytic activity of visible-light-induced C-doped TiO_2 catalyst for ethylene oxidation. *Chemical Engineering Journal*, 248: 175–183.

Lin, Y.T., Weng, C.H., Hsu, H.J., Huang, J.W., Srivastav, A.L. & Shiesh, C.C. 2014. Effect of oxygen, moisture, and temperature on the photo oxidation of ethylene on N-doped TiO_2 catalyst. *Separation and Purification Technology*, 134: 117–125. http://dx.doi.org/10.1016/j.seppur.2014.07.039

Lourenço, R.E.R.S., Linhares, A.A.N., de Oliveira, A.V., da Silva, M.G., de Oliveira, J.G. & Canela, M.C. 2017. Photodegradation of ethylene by use of TiO2 sol-gel on polypropylene and on glass for application in the postharvest of papaya fruit. *Environmental Science and Pollution Research*, 24(7): 6047–6054.

Malayeri, M., Haghighat, F. & Lee, C.S. 2021. Kinetic modeling of the photocatalytic degradation of methyl ethyl ketone in air for a continuous-flow reactor. *Chemical Engineering Journal*, 404(May 2020): 126602.

Malayeri, M., Haghighat, F. & Lee, C.-S. 2019. Modeling of volatile organic compounds degradation by photocatalytic oxidation reactor in indoor air: A review. *Building and Environment*, 154(January): 309–323.

Malayeri, M., Lee, C.S., Haghighat, F. & Klimes, L. 2020. Modeling of gas-phase heterogeneous photocatalytic oxidation reactor in the presence of mass transfer limitation and axial dispersion. *Chemical Engineering Journal*, 386(December 2019): 124013. https://doi.org/10.1016/j.cej.2020.124013.

Mamaghani, A.H., Haghighat, F. & Lee, C.S. 2018. Photocatalytic degradation of VOCs on various commercial titanium dioxides: Impact of operating parameters on removal efficiency and by-products generation. *Building and Environment*, 138(March): 275–282. https://doi.org/10.1016/j.buildenv.2018.05.002.

Mamaghani, A.H., Haghighat, F. & Lee, C.S. 2017. Photocatalytic oxidation technology for indoor environment air purification: The state-of-the-art. *Applied Catalysis B: Environmental*, 203: 247–269. http://dx.doi.org/10.1016/j.apcatb.2016.10.037.

Maneerat, C. & Hayata, Y. 2006. Efficiency of TiO_2 photocatalytic reaction on delay of fruit ripening and removal of off-flavors from the fruit storage atmosphere. *Transactions of the ASABE*, 49(3): 833–837.

Maneerat, C. & Hayata, Y. 2008. Gas-phase photocatalytic oxidation of ethylene with TiO_2-coated packaging film for horticultural products. *Transactions of the ASABE*, 51(1): 163–168.

Martínez-Romero, D., Bailén, G., Serrano, M., Guillén, F., Valverde, J.M., Zapata, P., Castillo, S. & Valero, D. 2007. Tools to maintain postharvest fruit and vegetable quality through the inhibition of ethylene action: A review. *Critical Reviews in Food Science and Nutrition*, 47(6): 543–560.

McCullagh, C., Skillen, N., Adams, M. & Robertson, P.K.J. 2011. Photocatalytic reactors for environmental remediation: A review. *Journal of Chemical Technology and Biotechnology*, 86(8): 1002–1017.

Mills, A. & Le Hunte, S. 1997. An overview of semiconductor photocatalysis. *Journal of Photochemistry and Photobiology A: Chemistry*, 108(1): 1–35.

Murshed, M.K., Dursun, A.Y. & Dursun, G. 2022. Application of response surface methodology on photocatalytic degradation of Astrazon Orange G dye by ZnO photocatalyst: Internal mass transfer effects. *Chemical Engineering Research and Design*, 188: 27–38.

Nayik, G.A. & Muzaffar, K. 2014. Developments in Packaging of Fresh Fruits-Shelf Life Perspective: A Review. *American Journal of Food Science and Nutrition Research*, 1(5): 34–39. http://www.openscienceonline.com/journal/fsnr

Nielsen, M.G., Vesborg, P.C.K., Hansen, O. & Chorkendorff, I. 2015. Removal of low concentration contaminant species using photocatalysis: Elimination of ethene to sub-ppm levels with and without water vapor present. *Chemical Engineering Journal*, 262: 648–657. http://dx.doi.org/10.1016/j.cej.2014.10.008

Nishizawa, T., Takeda, M., Murayama, H. & Matsushima, U. 2008. Effects of TiO_2 photocatalytic oxidation in the room atmosphere and the quality of tomato fruit during storage under a closed system. *Acta horticulturae*, 804: 309–314. http://www.actahort.org.

Obee, T.N. & Hay, S.O. 1997. Effects of moisture and temperature on the photooxidation of ethylene on titania. *Environmental Science and Technology*, 31(7): 2034–2038.

Parrino, F., Loddo, V., Augugliaro, V., Camera-Roda, G., Palmisano, G., Palmisano, L. & Yurdakal, S. 2019. Heterogeneous photocatalysis: guidelines on experimental setup, catalyst characterization, interpretation, and assessment of reactivity. *Catalysis Reviews - Science and Engineering*, 61(2): 163–213.

Passalía, C., Alfano, O.M. & Brandi, R.J. 2017. Integral design methodology of photocatalytic reactors for air pollution remediation. *Molecules*, 22(6): 1–17.

Pathak, N., Caleb, O.J., Geyer, M., Herppich, W.B., Rauh, C. & Mahajan, P.V. 2017. Photocatalytic and Photochemical Oxidation of Ethylene: Potential for Storage of Fresh Produce—a Review. *Food and Bioprocess Technology*, 10(6): 982–1001.

Pathak, N., Caleb, O.J., Rauh, C. & Mahajan, P. V. 2019. Efficacy of photocatalysis and photolysis systems for the removal of ethylene under different storage conditions. *Postharvest Biology and Technology*, 147(September 2018): 68–77.

Rawlings, J.B. & Ekerdt, J.G. 2002. *Chemical Reactor Analysis and Design Fundamentals*. Madison: Nob Hill Publishing.

Satuf, M.L., Brandi, R.J., Cassano, A.E. & Alfano, O.M. 2007. Scaling-up of slurry reactors for the photocatalytic degradation of 4-chlorophenol. *Catalysis Today*, 129: 110–117.

Sharmin, R. & Ray, M.B. 2012. Application of ultraviolet light-emitting diode photocatalysis to remove volatile organic compounds from indoor air. *Journal of the Air and Waste Management Association*, 62(9): 1032–1039.

Sirisuk, A., Hill, C.G. & Anderson, M.A. 1999. Photocatalytic degradation of ethylene over thin films of titania supported on glass rings. *Catalysis Today*, 54(1): 159–164.

Song, X., Wang, H., Li, Y., Ye, S. & Dionysiou, D.D. 2018. Solvothermal synthesis of P25/Bi 2 WO 6 nanocomposite photocatalyst and photocatalytic degradation of ethylene under visible light. *Applied Surface Science*, 439: 815–822.

Stroe, R.-E. & Rosendahl, L.A. 2019a. Kinetic study of the photocatalytic oxidation of ethylene over TiO_2 thin films. *IOP Conference Series: Materials Science and Engineering*, 628: 012009.

Stroe, R.-E. & Rosendahl, L.A. 2019b. Kinetic study of the photocatalytic oxidation of ethylene over TiO2 thin films. *IOP Conference Series: Materials Science and Engineering*, 628: 012009.

Syamsu, K., Warsiki, E., Yuliani, S. & Widayanti, S.M. 2016. Nano Zeolite-kmno4 as Ethylene Adsorber in Active Packaging of Horticulture Products (Musa Paradisiaca). *International Journal of Sciences: Basic and Applied Research (IJSBAR)*, 30(1): 93–103. http://gssrr.org/index.php?journal=JournalOfBasicAndApplied&page=article&op=view&path%5B%5D=6354

Terry, L.A., Ilkenhans, T., Poulston, S., Rowsell, L. & Smith, A.W.J. 2007. Development of new palladium-promoted ethylene scavenger. *Postharvest Biology and Technology*, 45(2): 214–220.

Tirgar, A., Han, D. & Steckl, A.J. 2018. Absorption of Ethylene on Membranes Containing Potassium Permanganate Loaded into Alumina-Nanoparticle-Incorporated Alumina/Carbon Nanofibers. *Journal of Agricultural and Food Chemistry*, 66(22): 5635–5643.

Tytgat, T., Hauchecorne, B., Abakumov, A.M., Smits, M., Verbruggen, S.W. & Lenaerts, S. 2012. Photocatalytic process optimisation for ethylene oxidation. *Chemical Engineering Journal*, 209: 494–500.

Visan, A., Rafieian, D., Ogieglo, W. & Lammertink, R.G.H. 2014. Modeling intrinsic kinetics in immobilized photocatalytic microreactors. *Applied Catalysis B: Environmental*, 150–151: 93–100.

Votruba, J., Sinkule, J., Hlaváček, V. & Skřivánek, J. 1975. Heat and mass transfer in monolithic honeycomb catalysts-I. *Chemical Engineering Science*, 30(1): 117–123.

Wills, R.B. & Golding, J.B. 2016. *Advances in Postharvest Fruit and Vegetable Technology*.

Wills, R.B.H., Harris, D.R., Spohr, L.J. & Golding, J.B. 2014. Reduction of energy usage during storage and transport of bananas by management of exogenous ethylene levels. *Postharvest Biology and Technology*, 89: 7–10. http://dx.doi.org/10.1016/j.postharvbio.2013.11.002.

Yamazaki, S., Tanaka, S. & Tsukamoto, H. 1999. Kinetic studies of oxidation of ethylene over a TiO2photocatalyst. *Journal of Photochemistry and Photobiology A: Chemistry*, 121(1): 55–61.

Ye, S. ying, Tian, Q. mei, Song, X. liang & Luo, S. can. 2010. Photoelectrocatalytic degradation of ethylene by a combination of TiO2 and activated carbon felts. *Journal of Photochemistry and Photobiology A: Chemistry*, 208(1): 27–35.

Zhang, J., Cheng, D., Wang, B., Khan, I. & Ni, Y. 2017. Ethylene Control Technologies in Extending Postharvest Shelf Life of Climacteric Fruit. *Journal of Agricultural and Food Chemistry*, 65(34): 7308–7319.

Zhang, Q., Ye, S., Chen, X., Song, X., Li, L. & Huang, X. 2017. Photocatalytic degradation of ethylene using titanium dioxide nanotube arrays with Ag and reduced graphene oxide irradiated by γ-ray radiolysis. *Applied Catalysis B: Environmental*, 203: 673–683.

Zhong, L. & Haghighat, F. 2015. Photocatalytic air cleaners and materials technologies e Abilities and limitations. *Building and Environment*, 91: 191–203. http://dx.doi.org/10.1016/j.buildenv.2015.01.033

Zorn, M.E., Tompkins, D.T., Zeltner, W.A. & Anderson, M.A. 2000. Catalytic and photocatalytic oxidation of ethylene on titania-based thin-films. *Environmental Science and Technology*, 34(24): 5206–5210.

APPENDIX: PROPOSED SENSOR DEVELOPMENT

Gas Sensor Development and Calibration

The gas sensor was developed using the MQ3 sensor module and Arduino UNO R3 board (Figure A.1). The development involved interfacing the MQ3 sensor module and other components into the Arduino board to build the circuit as depicted by the circuit diagram in Figure D.2. The circuit diagram was constructed using Cirkit Designer software. As shown in the circuit diagram, the Arduino board is underneath the data logging shield which has stacking headers so that it can be inserted into the pins of the Arduino board. The data logging shield is equipped with a real-time clock (RTC_DS1307) and an SD card compartment, thus the sensor data is timestamped with the current time and saved onto the SD card instantly.

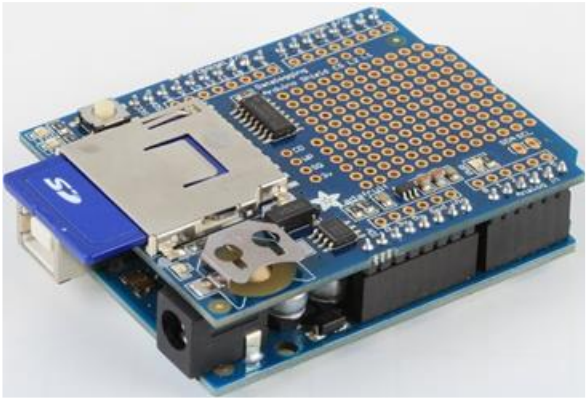

Figure A. 1: UNO R3 board mounted onto a data logging shield (Earl, 2023)

Other components of the circuit include the temperature and humidity sensor (DHT22), and the liquid crystal display (LCD,1602 I2C module). All these components were then programmed with Arduino IDE software, and the code is in section A.2. The MQ3 sensor does not measure the gas concentration directly but changes resistance depending on the concentration of the gas exposed to it. The calibration of the MQ3 gas sensor was done using an ethylene/ Air mix supplied by Air Products with cylinders of different concentrations of ethylene (10 ppm, 50 ppm, and 100 ppm). Before calibration, the MQ3 sensor was preheated by connecting the circuit to a power supply and leaving the sensor on for 48 hours. The setup for the calibration is in Figure A.3. For measurements, sampling bags were used to take gas samples from the cylinders into the vial in which the sensors were installed, as shown in Figure A.3. Firstly, clean synthetic air from Air Liquide was measured to determine the resistance (R_o), and then the different concentrations of ethylene were measured to determine the resistance

(R_s). Figure A.4 shows the obtained calibration curve. The equation obtained from the calibration curve was then included in the Arduino code to determine the concentration of ethylene.

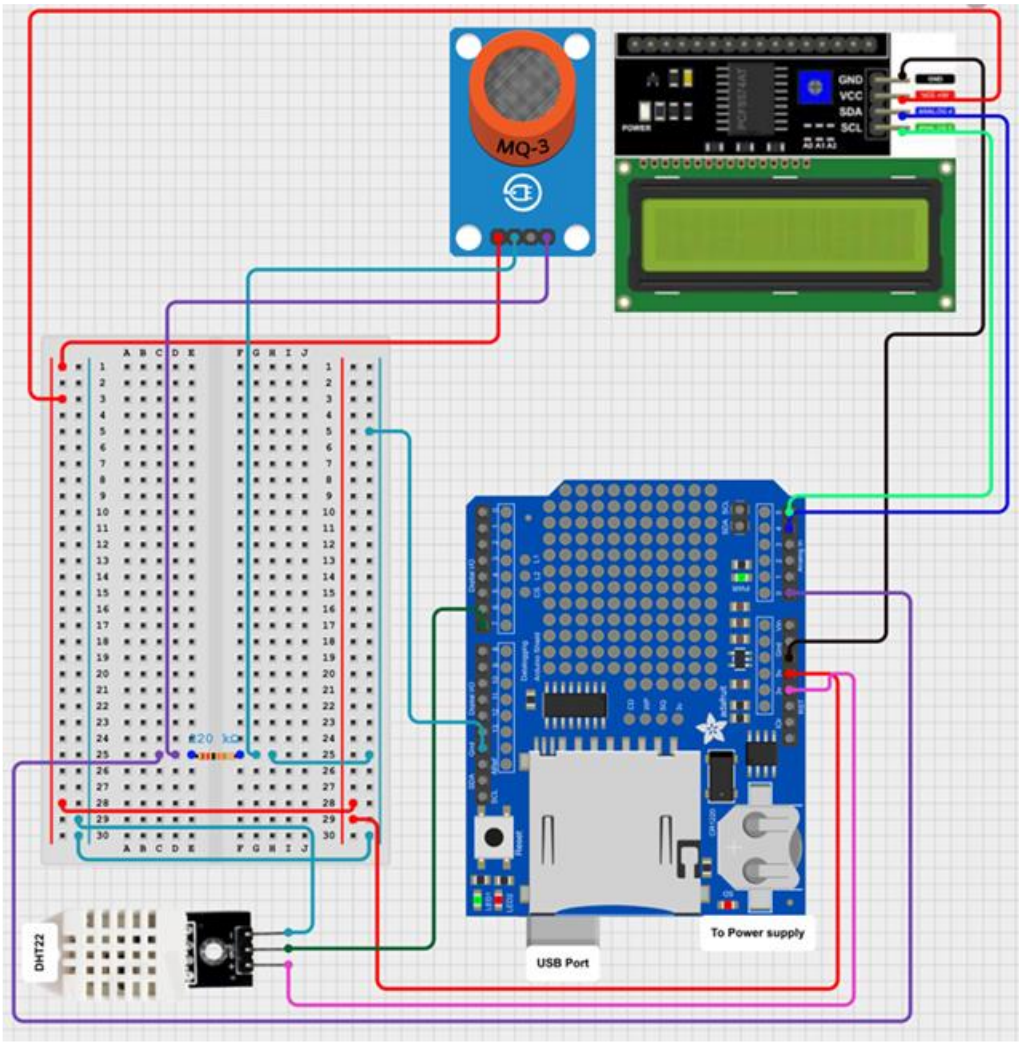

Figure A. 2: Sensor circuit diagram

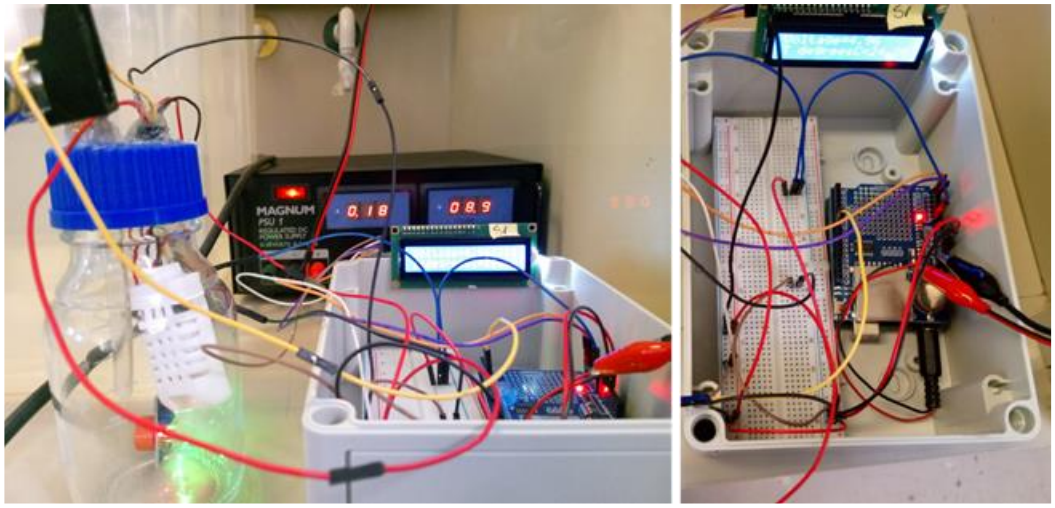

Figure A. 3: Sensor calibration setup

Arduino Code

```
#include <SPI.h>
#include <SD.h>
#include <DHT.h>;
#include "RTClib.h"

RTC_DS1307 rtc;

char daysOfTheWeek[7][12] = {"Sunday", "Monday", "Tuesday", "Wednesday",
"Thursday", "Friday", "Saturday"};

#include <LiquidCrystal_I2C.h>
LiquidCrystal_I2C lcd(0x3F, 16, 2);

int Air_sensorPin = A0;
#define DHTPIN 7
#define DHTTYPE DHT22
DHT dht(DHTPIN, DHTTYPE);

float Load_Resistance = 221000;
float Ro = 1484049.758;

File dataFile;

float Voltage;
float R;
float Air_sensorRead=0.0;
float ratio;
double C2H4ppm;
float Humidity;
float Temperature;
```

```
const int chipSelect = 10;

void setup()
{
   Serial.begin(9600);
pinMode(Air_sensorPin, INPUT);
dht.begin();
lcd.init();
lcd.backlight();

#ifndef ESP8266
  while (!Serial);
#endif

  if (! rtc.begin()) {
    Serial.println("Couldn't find RTC");
    Serial.flush();
    while (1) delay(10);
  }

  if (! rtc.isrunning()) {
    Serial.println("RTC is NOT running, let's set the time!");
       rtc.adjust(DateTime(F(__DATE__), F(__TIME__)));
      }


     Serial.print("Initializing SD card...");

  if(!SD.begin(chipSelect)) {
    Serial.println("initialization failed!");
    return;
  }
  Serial.println("initialization done.");

  dataFile = SD.open("C2H4ppm.txt", FILE_WRITE);

  if (dataFile) {
    Serial.println("File opened ok");
    dataFile.println("Date,Day,Time,Voltage,R,ratio,C2H4ppm,T degreesC,% RH");
  }
 dataFile.close();

  Serial.println("LABEL,Date,Day,Time,Voltage,R,ratio,C2H4ppm,T degreesC,%
RH");
}

void loop()
{
   int Air_sensorRead = analogRead(Air_sensorPin);
```

```
   float Voltage = Air_sensorRead*(5.0/1023.0);
   float R = ((5.0/Voltage)-1) * Load_Resistance;
   float ratio = R/Ro;
   double base = 10;
   double exponent = -1.3881-(20.534*log10(ratio));
   double C2H4ppm = pow(base,exponent);
   float Humidity = dht.readHumidity();
   float Temperature = dht.readTemperature();

     DateTime now = rtc.now();

    dataFile = SD.open("C2H4ppm.txt", FILE_WRITE);

  if (dataFile) {
    dataFile.print(now.year(), DEC);
    dataFile.print('/');
    dataFile.print(now.month(), DEC);
    dataFile.print('/');
    dataFile.print(now.day(), DEC);
     dataFile.print(",");

    dataFile.print(daysOfTheWeek[now.dayOfTheWeek()]);
    dataFile.print(",");

    dataFile.print(now.hour(), DEC);
    dataFile.print(':');
    dataFile.print(now.minute(), DEC);
    dataFile.print(':');
    dataFile.print(now.second(), DEC);
     dataFile.print(",");

    dataFile.print(Voltage,6);
    dataFile.print(",");

dataFile.print(R,6);
    dataFile.print(",");

dataFile.print(ratio,6);
    dataFile.print(",");

    dataFile.print(C2H4ppm,6);
    dataFile.print(",");

    dataFile.print(Temperature);
    dataFile.print(",");

    dataFile.print(Humidity);
    dataFile.print(",");

    dataFile.println();
```

```
    dataFile.close();
  }
  else
  Serial.println("SD card writing failed");

   Serial.println();

   Serial.print(now.year(), DEC);
    Serial.print('/');
    Serial.print(now.month(), DEC);
    Serial.print('/');
    Serial.print(now.day(), DEC);
     Serial.print(",");

    Serial.print(daysOfTheWeek[now.dayOfTheWeek()]);
    Serial.print(",");

    Serial.print(now.hour(), DEC);
    Serial.print(':');
    Serial.print(now.minute(), DEC);
    Serial.print(':');
    Serial.print(now.second(), DEC);
     Serial.print(",");

    Serial.print(Voltage,6);
       Serial.print(",");

Serial.print(R,6);
   Serial.print(",");

   Serial.print(ratio,6);
    Serial.print(",");

    Serial.print(C2H4ppm,6);
    Serial.print(",");

  Serial.print(Temperature);
    Serial.print(",");

    Serial.print(Humidity);
    Serial.print(",");

    dataFile.println();
    dataFile.close();

    lcd.clear();
    lcd.print("Voltage=");
   lcd.print(Voltage,6);
   lcd.setCursor(0,1);
 lcd.print("C2H4ppm=");
```

```
   lcd.print(C2H4ppm,6);

       dataFile.println();
    dataFile.close();
 delay(1000);
}
```

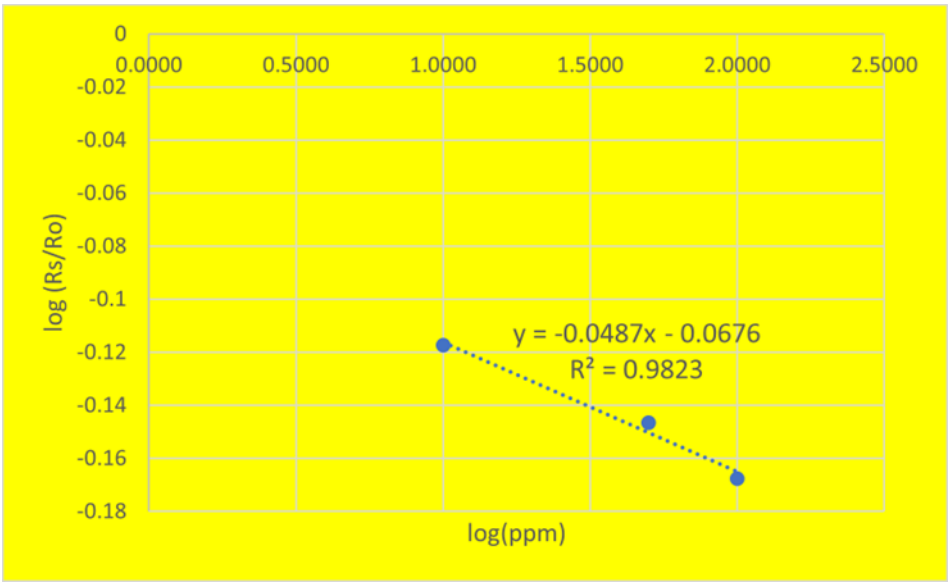

Figure A. 4: Sensor Calibration Curve